A Mixed-Flux-Based Nodal Discontinuous Galerkin Method for 3D Dynamic Rupture Modeling

Wenqiang Zhang[1], **Yajing Liu**[1], **Xiaofei Chen**[2,3]

[1]Department of Earth and Planetary Sciences, McGill University, Montréal, Québec, Canada
[2]Department of Earth and Space Science, Southern University of Science and Technology, Shenzhen, Guangdong, China
[3]Guangdong Provincial Key Laboratory of Geophysical High-Resolution Imaging Technology, Southern University of Science and Technology, Shenzhen, Guangdong, China

Key Points:

- We propose a mixed-flux-based nodal DG method to reduce dynamic rupture simulation dependence on mesh quality.
- Our method can handle various complexities in dynamic rupture simulations, as validated with published benchmark problem solutions.
- We present preliminary dynamic rupture modeling results for the 2008 Wenchuan earthquake and highlight the importance of fault geometry.

Corresponding author: Wenqiang Zhang, wenqiang.zhang@mcgill.ca

Abstract

Numerical simulation of rupture dynamics provides critical insights for understanding earthquake physics, while the complex geometry of natural faults makes numerical method development challenging. The discontinuous Galerkin (DG) method is suitable for handling complex fault geometries. In the DG method, the fault boundary conditions can be conveniently imposed through the upwind flux by solving a Riemann problem based on a velocity-strain elastodynamic equation. However, the universal adoption of upwind flux can cause spatial oscillations in cases where elements on adjacent sides of the fault surface are not nearly symmetric. Here we propose a nodal DG method with an upwind/central mixed-flux scheme to solve the spatial oscillation problem, and thus to reduce the dependence on mesh quality. We verify the new method by comparing our results with those from other methods on a series of published benchmark problems with complex fault geometries, heterogeneous materials, off-fault plasticity, roughness, thermal pressurization, and various versions of fault friction laws. Finally, we demonstrate that our method can be applied to simulate the dynamic rupture process of the 2008 Mw 7.9 Wenchuan earthquake along/across multiple fault segments. Our method can achieve high scalability in parallel computing under different orders of accuracy, showing high potential for adaptation to earthquake rupture simulation on natural tectonic faults.

Plain Language Summary

Numerical modeling of the earthquake rupture process helps us better understand and investigate the underlying physics of earthquakes. However, it remains challenging to model the fault rupture process for natural earthquakes, partially due to the geometric or/and geological complexities on/around the ruptured faults. To address these complexities, we develop a new numerical method for modeling the 3D fault rupture process of natural earthquakes. In this study we propose an improved, more flexible numerical scheme to reduce the dependency on mesh quality for earthquake rupture modeling and accommodate complex fault zone properties. We verify the correctness and efficiency of our method by benchmarking several typical models with complex fault geometries (e.g., branch faults and rough faults). We also apply our method to simulate the multi-fault rupture process of the 2008 Wenchuan earthquake to demonstrate the broad potential for natural earthquake modeling applications.

1 Introduction

In recent decades, numerical simulation of rupture dynamics has become a powerful means to study the underlying physics of earthquake source mechanisms. Seismogenic faults of natural earthquakes usually exhibit complex fault geometries such as dips, bends, branches, step-overs, and multi-fault coupling. For example, field investigations show the 2008 Wenchuan earthquake ruptured simultaneously on the two imbricate structures of the Beichuan and Pengguan fault (Xu et al., 2009). Seismic and geodetic data joint inversion illustrates the simultaneous ruptures on the plate interface and the overlaying splay faults on the 2016 Kaikōura earthquake (Wang et al., 2018). In addition, the medium around the fault also exhibits strong heterogeneity, which affects the earthquake rupture process. Ulrich et al. (2022) shows the importance of regional-scale structural heterogeneity to the hazards of the 2004 Sumatra–Andaman earthquake and Indian Ocean tsunami. These physical complexities place extremely high demands on the flexibility of numerical methods for rupture dynamics.

Earlier modelings of earthquake dynamic rupture use the semi-analytical boundary integration equation method (BIEM) (Das, 1976; Das & Aki, 1977). BIEMs are flexible in modeling geometric complex faults (Ando & Kaneko, 2018; Qian et al., 2019) but limited to homogeneous media. Therefore, pure numerical methods such as finite differ-

ence methods (FDMs) (Madariaga, 1976; Day, 1982), finite volume methods (FVMs) (Benjemaa et al., 2009) and finite element methods (FEMs) (Barall, 2009; Aagaard et al., 2013) are applied to three-dimensional (3D) dynamic rupture modelings. The FDM, especially the staggered-grid FDM (Day et al., 2005; Dalguer & Day, 2007), has a simple numerical scheme and high computational efficiency and is one of the most widely used methods. To overcome the limitations of these traditional FDMs on modeling geometrically complex faults, curvilinear FDMs (Kozdon et al., 2012; Z. Zhang et al., 2014; W. Zhang et al., 2020) are developed, which can handle more complex faults such as non-planar faults. Combined with multi-block grid technology, FDMs can model geometric complex megathrust earthquakes such as the 2011 Tohoku-Oki earthquake (Kozdon et al., 2013; Kozdon & Dunham, 2013).

Despite the high efficiency of FDMs and hexahedral-mesh-based FEMs (Ely et al., 2009; Kozdon et al., 2013; Z. Zhang et al., 2014; Galvez et al., 2014; Duru et al., 2021), it remains challenging for dynamic rupture modeling with geologically and geometrically complex faults. In contrast, the meshing process for tetrahedral meshes is automatic and more user-friendly even with open-source meshing software (Geuzaine & Remacle, 2009; Si, 2015). Therefore, tetrahedral mesh-based numerical methods for 3D rupture dynamics are developed, including FEMs (Oglesby et al., 2000; Ma & Archuleta, 2006; Aagaard et al., 2013), FVMs (Benjemaa et al., 2009) and discontinuous Galerkin (DG) methods (also called discontinuous FEM) (Pelties et al., 2012; Tago et al., 2012; Ye et al., 2020). Among them, the DG method combines the high-order advantages of the FEM with the advantages of the easy parallelization of the FVM and has become a competitive method for rupture dynamics. In DG methods, numerical flux is used for implementing various boundary conditions (Cockburn et al., 2012; Hesthaven & Warburton, 2008). The upwind flux (one type of numerical flux) (de la Puente et al., 2009) can inherently suppress artificial high-frequency oscillations without adding artificial viscosity, which is used in many traditional FEMs (e.g., Aagaard et al. (2013); Galvez et al. (2014)).

In this work, we develop a new method for 3D dynamic rupture modelings based on the Gauss-Lobatto-Legendre-based nodal discontinuous Galerkin (NDG) framework (Hesthaven & Warburton, 2008) and apply it to model natural earthquakes with multiple faults. We use the velocity-strain form of the elastodynamic equation, which can better describe multi-geophysical problems such as acoustic-elastic coupling under the unified framework (Wilcox et al., 2010; Ye et al., 2016). For the first time, we derive an upwind flux formulation in the form of a velocity-strain equation to impose fault boundary conditions for dynamic rupture problems. The framework of upwind-flux-based on the velocity-strain equation has been extended to model seismic waves in more complex cases (e.g., anisotropy, viscoelasticity) (Zhan et al., 2020). Therefore, the use of the velocity-strain equation facilitates us to continue to incorporate these complexities to dynamic rupture problems in the future. The NDG method we use here is mathematically equivalent to the modal DG method but different in terms of computation (Hesthaven & Warburton, 2008). Extra conversions of the modal and nodal coefficients are required in the modal DG framework for the implementation of Drucker–Prager viscoplasticity (Wollherr et al., 2018). In contrast, the viscoplasticity can be straightforwardly incorporated in the NDG framework, which greatly simplifies the numerical implementation.

The upwind flux is advantageous in suppressing spurious high-frequency oscillations, resulting in smooth and accurate simulated time series of the rupture process (de la Puente et al., 2009). However, in some dynamic rupture modeling cases, universal adopting upwind flux for all boundary conditions can be problematic. If the mesh adjacent to the fault is not approximately symmetric, the use of upwind flux can lead to spatially oscillating results, especially in the normal or shear stress components. This phenomenon is not a bug in the code implementation, as a similar phenomenon also occurs in the modal DG method using upwind flux (Breuer & Cui, 2016, 2018). The existence of this problem makes mesh generation for dynamic rupture problems challenging. For some sim-

ple geometries, such as a vertical planar fault, we can construct a mirrored mesh to make sure the mesh is symmetric to the fault surface, resulting in oscillation-free simulation results. While for non-planar faults or low-dip-angle thrust faults, it is impossible to generate an ideally symmetric mesh and challenging to generate a nearly symmetric mesh. To solve this problem, we propose a mixed flux scheme, that is, using a mixture of upwind fluxes and central fluxes. The benchmark examples we tested show that the mesh-induced spatial oscillations in the upwind-flux-based DG method are removed after using our proposed mixed flux scheme. Therefore, by using our improved DG method with mixed flux, we reduce the dependence on mesh quality, enabling modelers to choose more mesh generation software for constructing complex fault models.

We tested our NDG method with MPI and found good parallel scalability for tests up to about 500 CPU processors. At the current stage, the parallel scalability of this method has enabled us to simulate the rupture dynamics of various complex fault systems of large earthquakes, and our method holds the potential to adapt to a larger parallel scale in supercomputers (Fu et al., 2017). By comparing with benchmark examples from "The SCEC/USGS Spontaneous Rupture Code Verification Project" (Harris et al., 2009, 2018), we verify the accuracy and flexibility of our method in modeling rupture dynamics with the bimaterial property, branched faults, off-fault plasticity, fault roughness, thermal pressurization and various friction laws. Finally, we demonstrate the preliminary dynamic rupture modeling of the complex fault system of the 2008 Wenchuan earthquake. We include topography and complex geometries with multi-faults in our simulations. The multi-fault system of the Wenchuan earthquake includes the Beichuan fault, Pengguan fault and Xiaoyudong fault (Xu et al., 2009). By using the method developed in this work, we further added the Xiaoyudong fault, which is confirmed to be ruptured during the earthquake but was difficult to be incorporated in previous simulations (Tang et al., 2021). Both benchmark models and the Wenchuan earthquake model illustrate the advantages of this method in simulating dynamic rupture process of complex fault systems.

2 The Nodal Discontinuous Galerkin Method

In this section, we show the framework of the NDG method, and demonstrate how to implement fault boundary conditions by solving exact Riemann problems under the velocity-strain form of elastodynamic equations.

2.1 DG Discretization

We consider an elastic media in this work. A velocity-strain form of elastodynamic equations is adopted, which is suitable to describe multi-physics problems under the same unified framework (Wilcox et al., 2010; Ye et al., 2016; Zhan et al., 2020). In the velocity-strain DG framework, the solution vector is consists of velocity and strain variables:

$$\boldsymbol{q} = (\rho v_x, \rho v_y, \rho v_y, \epsilon_{xx}, \epsilon_{yy}, \epsilon_{zz}, \epsilon_{yz}, \epsilon_{xz}, \epsilon_{xy})^T, \tag{1}$$

where ρ is density, v_i is the particle velocity, ϵ_{ij} is the strain and γ_{ij} is the engineering strain ($\gamma_{ij} = \frac{1}{2}\epsilon_{ij}$). Let Ω denote the computational domain (Figure 1). Ω is discretized into N_e non-overlapping tetrahedral elements $\Omega_i (i = 1, 2, ..., N_e)$ with the boundary $\partial\Omega_i$. The solution vector in each element Ω_i is approximated as:

$$q_i(r, t) = \sum_{k=1}^{N_p} q_{i,k}(t) l_k(r), \tag{2}$$

here l_k is the nodal Lagrangian basis function with the maximum number of $N_p = \frac{N(N+1)(N+2)}{6}$, N is the polynomial order. Therefore, the expansion coefficients $q_{i,k}$ are also the nodal solution variables on the collocation points r on Ω_i. Following the classic workflow of DG method (Text S1-S2 in Supporting Information S1), we apply the DG testing (set test

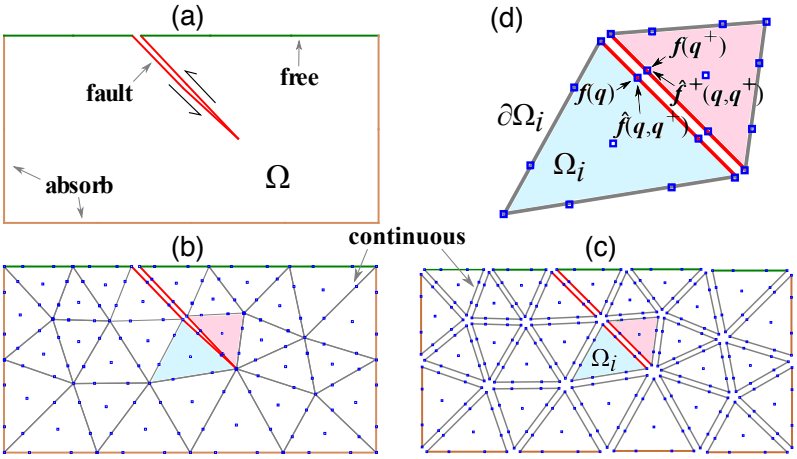

Figure 1. (a) A 2D schematic dynamic rupture model, Ω denotes the entire computational domain, including the fault (red lines), free (green lines) and absorbing boundaries (magenta lines). (b) The continuous Galerkin (traditional FEM) discretization, solution vectors $\boldsymbol{q}$ are defined in the nodal points (blue squares). Fault surfaces are represented as "split nodes" (points share locations but have double values), and continuous boundaries (gray lines) are represented as shared points. (c) The discontinuous Galerkin (DG) discretization, both fault and continuous boundaries are represented as "split nodes". (d) The element Ω_i with three boundaries $\partial\Omega_i$ and one of its neighbouring element. $\boldsymbol{f}(\boldsymbol{q})$, $\boldsymbol{f}(\boldsymbol{q}^+)$ are the flux function vectors. $\hat{\boldsymbol{f}}(\boldsymbol{q},\boldsymbol{q}^+)$, $\hat{\boldsymbol{f}}^+(\boldsymbol{q},\boldsymbol{q}^+)$ are the "numerical" flux vectors, which are used to implement all boundary conditions in the DG framework.

function as basis function) to the velocity-strain form of elastodynamic equations:

$$\int_{\Omega_i} l_k[\partial_t \boldsymbol{q} - \nabla\cdot(\boldsymbol{f},\boldsymbol{g},\boldsymbol{h})]\mathrm{d}V = \int_{\partial\Omega_i} l_k T^{-1}(\hat{\boldsymbol{f}}-\boldsymbol{f})\mathrm{d}S, \tag{3}$$

here $\boldsymbol{f},\boldsymbol{g},\boldsymbol{h}$ is the flux functions in the x,y,z directions:

$$\begin{aligned}\boldsymbol{f} &= (\tau_{xx},\tau_{xy},\tau_{xz},v_x,0,0,0,v_z,v_y)^T,\\ \boldsymbol{g} &= (\tau_{xy},\tau_{yy},\tau_{yz},0,v_y,0,v_z,0,v_x)^T,\\ \boldsymbol{h} &= (\tau_{xz},\tau_{yz},\tau_{zz},0,0,v_z,v_y,v_x,0)^T,\end{aligned} \tag{4}$$

where $\hat{\boldsymbol{f}}$ is the "numerical" flux, which is a combination of the solution vectors in the split faces of the two adjacent elements: $\hat{\boldsymbol{f}} = \hat{\boldsymbol{f}}(\boldsymbol{q},\boldsymbol{q}^+)$ (see Figure 1, the superscript "+" indicates the neighboring elements). Numerical flux is the core of the FVM and DG methodologies (LeVeque, 2002; Toro, 2009). T is the rotation matrix which is used to rotate the global coordinate to the element face aligned local coordinate (Text S3 in Supporting Information S1) for the convenience of deriving the numerical flux. Note that the flux $\boldsymbol{f},\hat{\boldsymbol{f}}$ in the right term of the Equation 3 is in the local coordinate. Once the numerical flux $\hat{\boldsymbol{f}}$ is derived in the local coordinate, it should be rotated back into the global coordinate using the inverse rotation matrix T^{-1}.

2.2 Boundary Conditions

How to implement the boundary conditions is crucial for developing numerical methods for dynamic rupture models. There are four types of boundary conditions in the model (Figure 1): 1) fault surface, where the elements have relative motion (dislocation); 2) free surface, where the traction force vanishes; 3) absorbing boundaries of the model domain,

where inward-going waves are vanished; 4) continuous boundaries, unbroken elements without relative motion. In the continuous Galerkin (traditional FEM) framework, continuous boundary conditions are implicitly implemented as the solution/flux vectors in the boundary share the same value: $\boldsymbol{q} = \boldsymbol{q}^+$, $\boldsymbol{f}(\boldsymbol{q}) = \boldsymbol{f}(\boldsymbol{q}^+)$. While in the DG framework, all interior boundaries (including continuous boundaries) are represented as split nodes with double values, i.e., $\boldsymbol{f} \neq \boldsymbol{f}^+$ holds even for continuous boundary conditions (Figure 1d). All the boundary conditions are implemented in the numerical flux term (e.g., $\hat{\boldsymbol{f}} = \hat{\boldsymbol{f}}^+$ for continuous boundary conditions), rather than the flux term $\boldsymbol{f}$.

In this work, we choose the upwind flux for the numerical flux term $\hat{\boldsymbol{f}}$ (Equation 3) for its advantage for suppressing spurious high-frequency oscillations (de la Puente et al., 2009). However, in Section 3, we show that the universal adoption of the upwind flux for all boundary conditions can be problematic in some dynamic rupture cases and a modification of upwind flux will be introduced. In the following two subsections, we start to derive the upwind flux for a dynamic rupture model by introducing the Riemann solvers.

2.2.1 Riemann Solver for Continuous Boundaries

Following the framework of Toro (2009); Zhan et al. (2020), assuming x is the normal direction of the element boundary, we solve the Riemann problem under the Rankine-Hugoniot conditions (Text S4.1 in Supporting Information S1) for the continuous boundary condition ($\hat{\boldsymbol{f}}^+ = \hat{\boldsymbol{f}}$):

$$[\![\hat{v}_\theta]\!] = 0, [\![\hat{\tau}_{x\theta}]\!] = 0, (\theta = x, y, z), \tag{5}$$

yielding the upwind flux:

$$\hat{\boldsymbol{f}} - \boldsymbol{f} = (Z_p\alpha_1, Z_s\alpha_2, Z_s\alpha_3, \alpha_1, 0, 0, 0, \alpha_3, \alpha_2)^T, \tag{6}$$

where $\alpha_1 = \frac{[\![\tau_{xx}]\!]+Z_p^+[\![v_x]\!]}{Z_p+Z_p^+}$, $\alpha_2 = \frac{[\![\tau_{xy}]\!]+Z_s^+[\![v_y]\!]}{Z_s+Z_s^+}$, $\alpha_3 = \frac{[\![\tau_{xz}]\!]+Z_s^+[\![v_z]\!]}{Z_s+Z_s^+}$, Z_p, Z_s are the impedance of P and S waves. The superscript "+" indicates the neighboring elements. $[\![\cdot]\!]$ denotes the difference between the solutions on the face of two adjacent elements: $[\![\theta]\!] \equiv \theta^+ - \theta$. For the free surface boundaries and the exterior boundaries, Equation 6 is also used by setting the artificial solution vector $\boldsymbol{q}^+$ as stress imaged solution ($\tau_{x\theta}^+ = -\tau_{x\theta}, \theta = x, y, z$) or vanished solution ($\boldsymbol{q}^+ = 0$), respectively.

2.2.2 Riemann Solver for Ruptured Boundaries

The spontaneous rupture problem requires mixed continuous-discontinuous boundary conditions, i.e., $\hat{\boldsymbol{f}}^+ \neq \hat{\boldsymbol{f}}$ (the stress components are continuous while the velocities are discontinuous). We rotate the coordinate to set the fault normal direction as x, hence the fault slips at y and z direction. Then the fault boundary conditions are expressed using the numerical flux as follows:

$$[\![\hat{v}_x]\!] = 0, [\![\hat{v}_y]\!] = V_y, [\![\hat{v}_z]\!] = V_z, [\![\hat{\tau}_{x\theta}]\!] = 0, (\theta = x, y, z). \tag{7}$$

Solving the Riemann problem for rupture boundary conditions (Text S4.2 in Supporting Information S1) yields the following relationship:

$$\hat{\tau}_{x\theta} = \Phi_\theta - \eta V_\theta, (\theta = y, z), \tag{8}$$

where $\eta = \frac{Z_s Z_s^+}{Z_s+Z_s^+}$. Φ_θ is the shear stress component when the fault is locked (Equation 9, $\Phi_y = Z_s\alpha_2$, $\Phi_z = Z_s\alpha_3$). Applying the parallel condition $\frac{\tau}{|\tau|} = \frac{\mathbf{V}}{|\mathbf{V}|}$, we obtain the relationship for the absolute slip rate V and shear stress τ:

$$\hat{\tau} = \Phi - \eta V. \tag{9}$$

Equation 9 is crucial for implementing fault boundary conditions. Combining Equation 9 and the friction laws, we can solve the stress shear and the slip rate on the fault. Next, we will illustrate the details for implementing slip weakening and rate-state friction laws.

For slip weakening friction law, the friction coefficient is slip dependent:

$$\mu_f = \mu_f(s) = \max\{\mu_d, (\mu_s - \mu_d)\frac{s}{D_c}\}, \tag{10}$$

where μ_s, μ_d is the static and dynamic friction, D_c is the characteristic slip distance. s is the fault slip which can be obtained by integrating fault slip rate V. The fault normal stress is solved by implementing the continuous and the "non-open" condition:

$$\sigma = \min\{0, \hat{\tau}_{xx} + \tau^0_{xx}\}, \tag{11}$$

the superscript "0" in τ^0_{xx} denotes prestress. $\hat{\tau}_{xx}$ is the numerical flux of the normal stress component when the fault is locked. From Equation 6 we can know $\hat{\tau}_{xx} = Z_p\alpha_1$. If $\hat{\tau} = \sqrt{\hat{\tau}^2_{xy} + \hat{\tau}^2_{xz}}$ is larger than the shear strength $\mu_f\sigma$, which means that the fault cannot remain locked and begins to slip, then the shear stress should be $\mu_f\sigma$. Otherwise, when the fault stress τ is below the level of the fault strength, indicating the fault is locked, the absolute fault shear stress should be $\hat{\tau}+\hat{\tau}^0$. The formula of relative fault stress under these two circumstances can be summarized as the following equation:

$$\hat{\tau} = \min\{\hat{\tau}, \mu_f\sigma - \tau^0\}, (\theta = y, z). \tag{12}$$

Once we obtain the shear stress, the slip rate can be solved by the relationship between shear stress and slip rate (Equation 9).

For rate-state friction laws, since the fault is always sliding, then we can directly set the shear stress as $\mu_f\sigma$. Combined with Equation 9, a nonlinear equation can be obtained:

$$\hat{\tau} = \Phi - \eta V = \mu_f(V, \psi)\sigma. \tag{13}$$

In this case, the friction μ_f is rate (V) and state (ψ) dependent. A nonlinear solver, such as Newton-Rasphson or Regula Fasi, can be used to solve the slip rate V in Equation 13. The state variable ψ, obeying different evolution laws: $\frac{\mathrm{d}\psi}{\mathrm{d}t} = G(V, \psi)$, is updated by the same time integration method for solution vector $\boldsymbol{q}$. In this work, the time integration method is the fourth-order low-storage Runge-Kutta method (Carpenter & Kennedy, 1994).

3 Method Improvement

In this section, we will demonstrate that the upwind flux introduced in the previous section is problematic when the near-fault mesh is not nearly symmetric in some modeling cases. We then propose a new mixed flux scheme to improve the performance of the DG method for dynamic rupture modeling.

3.1 The Problematic Upwind Flux in Rupture Dynamics

To show the upwind flux is a double-edged sword for dynamic rupture modelings, we start with its advantages. The upwind flux is intensively used in wave propagation problems (Käser & Dumbser, 2006; Wilcox et al., 2010; Zhan et al., 2020) for its inherent dissipation effect and hence free of spurious high-frequency oscillations. de la Puente et al. (2009) first applied the upwind-flux-based modal DG method to dynamic rupture modeling and demonstrated that this method is free of spurious high-frequency oscillations without artificial damping (Kaneko et al., 2008). Figure 2 shows the different oscillation behaviours of the upwind-flux DG method and the SEM. Using a non-dissipative central flux have similar spurious high-frequency oscillation problem (Tago et al., 2012,

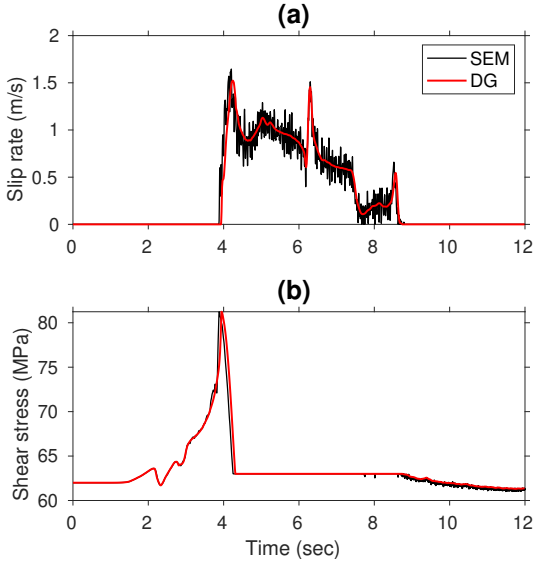

Figure 2. An example showing the spurious high-frequency oscillations using the SCEC/USGS dynamic rupture benchmark problem TPV5. (a) Slip rate (b) shear stress time series on a station of fault surface, which is 7.5 km away from the nucleation center along strike, and at the same depth as the nucleation center. The black color indicates the results of the SEM (Kaneko et al., 2008) and the red color is calculated by a modal DG method (Pelties et al., 2012).

Figure 9 therein) as the SEM. These studies show the use of upwind flux is advantageous for suppressing the spurious high-frequency oscillations in dynamic rupture modeling.

However, we found that the use of the upwind flux results in other types of numerical "oscillations" under certain circumstances. As shown in Figure 3, when the mesh adjacent to the fault is not symmetric, the use of upwind flux is prone to spatial oscillations, especially in the stress components. To avoid confusion and to distinguish it from the "spurious high-frequency oscillation" described in Figure 2, we name the oscillations in Figure 3 as "spatial spikes". The spatially oscillated "spikes" are not oscillated in the time series but are deviated from true values (Figure 2e,2f). The spurious high-frequency oscillations (Figure 2) are mesh-independent and can be suppressed by adding the artificial damping (e.g. Kelvin-Voigt viscosity), and it does not lead to numerical instabilities and can be reduced by mesh refinement. In contrast, the "spatial spikes" (Figure 3) is mesh-dependent and can lead to serious instability, especially when the mesh size is refined and/or the polynomial order increases since the "filtering effect" by the dissipation of the upwind flux is less.

The phenomenon of "spatial spikes" exists not only in our nodal DG method based on the velocity-strain equation, but also in the modal DG (ADER-DG) method based on the velocity-stress equation (Pelties et al., 2012). There are two independent implementations for the ADER-DG method, SeisSol and EDGE. Breuer and Cui (2016) reported that the "spatial spaikes" exists in both implementations, which indicates a "troubled numerical" scheme rather than a bug in the actual implementation. Our numerical implementation is completely different from SeisSol or EDGE since our method is based on the velocity-strain nodal DG framework (Hesthaven & Warburton, 2008). Therefore, the fact that "spatial spikes" exist in both methods (Figure 3) Breuer and Cui (2016, Figure 4) further confirms the problem of the upwind-flux-based numerical scheme. Breuer and Cui (2018) tried to solve this problem by using limiters, which is commonly used

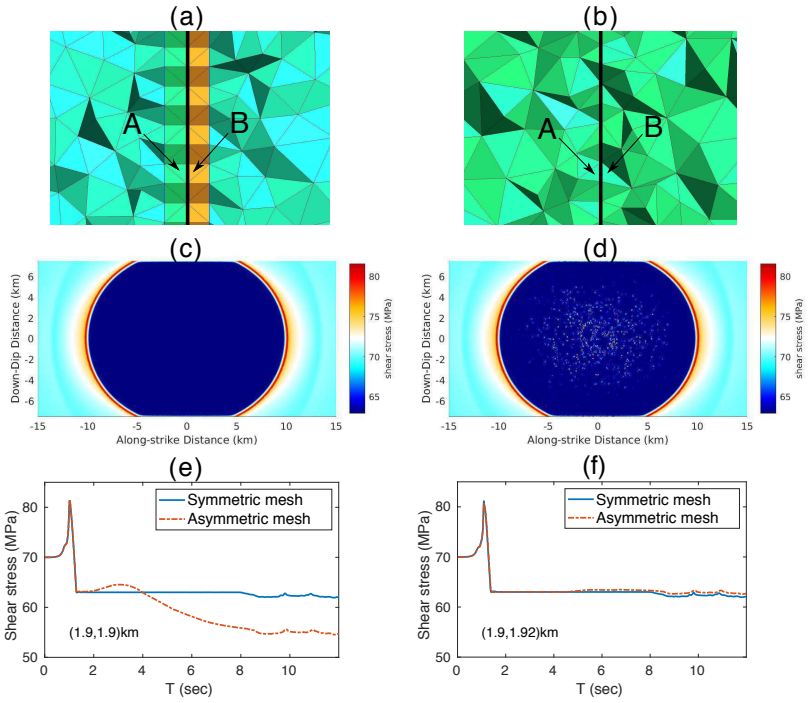

Figure 3. An example showing the mesh induced "spatial spikes". (a) and (b) are cross sections perpendicular to the fault plane. (a) symmetric mesh with an extruded layer; (b) asymmetric mesh without an extruded layer. A and B are two neighbouring elements which are immediately adjacent to the fault. Both meshes are generated by the Gmsh software (Geuzaine & Remacle, 2009) and strong mesh coarsening is applied (The edge length of the element size near the fault is 200 m, and increases to 5 km at the domain boundary). The "frontal-Delaunay" algorithm is used to generate the 2D surface mesh and the "Delaunay" algorithm to generate the 3D volumetric mesh. (c) and (d) are the snapshots of shear stress at time 4 seconds calculated with mesh (a) and (b). (e) and (f) show the comparison of shear stress time series calculated by the symmetric (a) or asymmetric (b) mesh. (e) and (f) are results of two nearby stations: (1.9 km,1.9 km) and (1.9 km, 1.92 km) (the first number is along-strike distance and the second is along dip distance).

in DG methods to deal with numerical oscillations caused by the non-linearity of the equations (Dumbser & Loubère, 2016). However, as we show in the following, this phenomenon is not caused by non-linearity, therefore adding a limiter does not remove the spatial spikes, as confirmed by their test results (Breuer & Cui, 2018). We show in the next section that this phenomenon is caused by the upwind flux and a modification of the upwind flux treatment can remove such spatial spikes.

We need to emphasize that the "spatial spikes" instability only occurs when certain types of meshes are involved. Based on the comparison in Figure 3, we found the asymmetry of the mesh adjacent to the fault are the most important contributing factor. Therefore, we define a parameter to measure the mesh quality for dynamic rupture models:

$$r_v \equiv \max\{\frac{V_A}{V_B}, \frac{V_B}{V_A}\}, \tag{14}$$

where A and B are the pair of neighbouring elements adjacent to the fault surface (Figure 3a, 3b), V_A and V_B are respective volumes and r_v is the volume ratio. When the el-

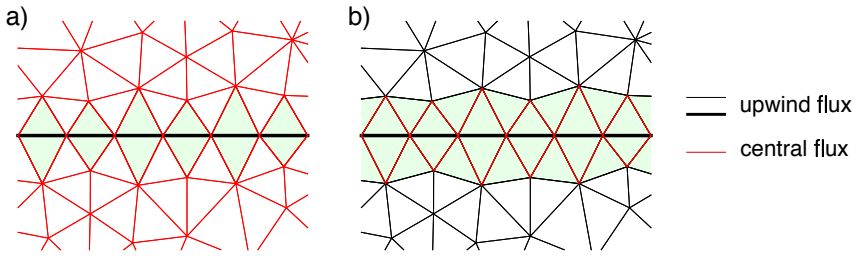

Figure 4. A 2D schematic illustration for the scheme of (a) "mixed flux 1" and (b) "mixed flux 2". The fault surface is highlighted by the thick black line. The light green color indicates the elements using mixed fluxes. In each light green element, the upwind flux are used for the black edges (including the fault), while the central flux are used for the red edges. In this 2D example, a total of 3090 edges require numerical flux to implement boundary conditions. For (a), 2994 edges (97%) use central flux (red color); for (b), only 250 edges (8%) use central flux (red color).

311 ements adjacent to the fault are completely symmetric (Figure 3a), the volume ratio is
312 1. When the volume ratio is much larger than 1, it indicates that the elements adjacent
313 to the fault are very asymmetric (Figure 3b), which leads to the instability shown in Fig-
314 ure 3d. While a perfectly symmetric mesh is ideal, for many non-planar faults it is very
315 difficult to achieve. In our experience, when $r_v > 1.5$, instabilities like Figure 3d will
316 occur. For 3D dynamic rupture problems, the use of unstructured triangular meshes can-
317 not always guarantee that $r_v < 1.5$, especially when the strong mesh coarsening strat-
318 egy is implemented. This suggests that the problem of upwind flux in rupture dynam-
319 ics needs to be addressed.

320 ### 3.2 The Mixed Flux

321 Here we introduce a "mixed flux" scheme to improve the performance of the up-
322 wind flux in dynamic rupture modelings. Mixed flux, as the name suggests, is a mix of
323 upwind flux and other flux (here, the central flux). The application of specific types of
324 numerical flux schemes will be dependent on the types of boundary conditions. Figure
325 4 is a schematic diagram of our proposed mixed flux method. In the first scenario "mixed
326 flux 1", We use central flux for all the continuous boundary conditions (Equation 6):

327 $$\hat{\boldsymbol{f}}(\boldsymbol{q}, \boldsymbol{q}^+) = \frac{\boldsymbol{f}(\boldsymbol{q}) + \boldsymbol{f}(\boldsymbol{q}^+)}{2} \tag{15}$$

328 while keep the upwind flux for the rest of the boundaries, including the fault surfaces,
329 free surfaces, and absorbing boundaries (Figure 4a). But since most of the element bound-
330 aries are continuous boundaries, "mixed flux 1" (Figure 4a) results in an extremely high
331 proportion (e.g., 97% in the case of Figure 4a) of central flux usage. That is, the mixed
332 flux 1 is close to the central flux method, which is prone to spurious high-frequency os-
333 cillations (Tago et al., 2012) (note that it is different from the spatial spikes discussed
334 in previous section). To solve this problem, we propose a more advantageous "mixed flux
335 2" scheme by limiting the use of the central flux only on the surfaces immediately ad-
336 jacent to the fault, while for other surfaces the upwind flux is still used to impose con-
337 tinuous boundary conditions (Figure 4b). We use the following two examples to demon-
338 strate the second mixed flux scheme can greatly reduce the dependence of mesh qual-
339 ity when modeling a dynamic rupture process.

340 The first example is SCEC/USGS Spontaneous Rupture Code Verification TPV3,
341 spontaneous rupture on a vertical right-lateral strike-slip fault in a homogeneous full space

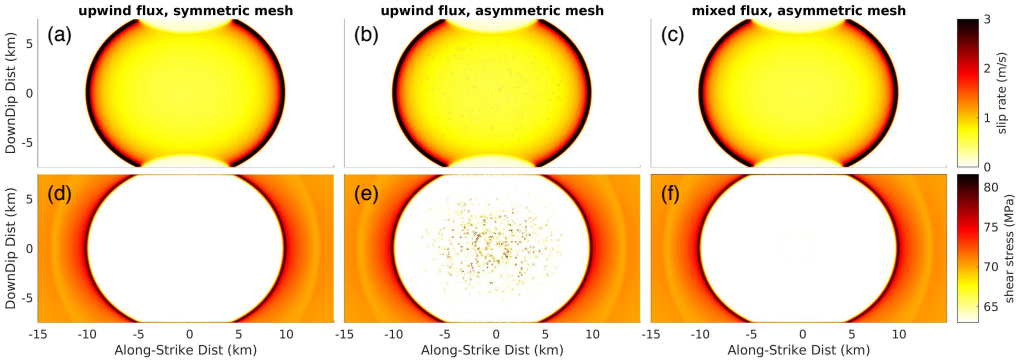

Figure 5. Comparison of results calculated by different numerical flux schemes and different meshes. Top and bottom rows show snapshots of slip rate and shear stress, respectively, at 4 second. (a), (d): symmetric mesh + upwind flux; (b), (e): asymmetric mesh + upwind flux; (c), (f): asymmetric mesh + mixed flux (Figure 4b).

(Harris et al., 2009). This benchmark problem has been used by many studies to verify numerical results (Pelties et al., 2012; Tago et al., 2012; Z. Zhang et al., 2014). The fault surface is vertical and planar with a size of 30 km by 15 km. The initial stress is 70 MPa in the strike direction, and 0 MPa in the down-dip direction. The central area is the nucleation zone with a size of 3 km by 3 km and initial stress of 81.6 MPa. The initial normal stress is 120 MPa on the entire fault surface. Linear slip weakening friction law is used with the parameters $\mu_s = 0.677$, $\mu_d = 0.525$ and $D_c = 0.4$ m. The material is homogeneous: $V_p = 6$ km/s, $V_s = 3.464$ km/s, and $\rho = 2.67$ g/cm^3. To illustrate the effect of mesh quality on the rupture process, two meshes are generated using the Gmsh software (Geuzaine & Remacle, 2009). For the first mesh, we add two extra layers, one on each side of the fault surface, to ensure that each pair of element adjacent to the fault are completely symmetric (Figure 3a). Therefore, the volume ratio r_v is 1 on the entire fault surface. As a comparison group, the second mesh does not include the extra layers on both sides of the fault surface (Figure 3b). Therefore, the volume ratio r_v of many pairs of elements immediately adjacent to the fault surface exceeds 1.5. We use the "frontal-Delaunay" algorithm to generate the 2D surface mesh and the "Delaunay" algorithm to generate the 3D volumetric mesh. Both meshes use strong mesh coarsening. The edge length of the elements near the fault is 200 m, and is coarsened to 5 km at the domain boundary. We use the spatial order of $O = 3$ to perform the simulations.

We first calculate the results using upwind flux and a symmetric mesh, as shown in Figures 5a and 5d. The results show that both the slip rate and the shear stress are smooth, with no spatial oscillations, suggesting that upwind flux is a suitable choice when the mesh quality is good. By contrast, the application of upwind flux to an asymmetric mesh leads to severe spatial oscillations (Figure 5b, 5e). The spatial oscillation disappears with the mixed flux strategy despite the asymmetric mesh (Figure 5c, 5f), generating slip rate and shear stress distributions very similar to those using the upwind flux with symmetric mesh (Figure 5a, 5d). This shows that our improved mixed flux can achieve satisfactory results even with asymmetric meshes, whereas the upwind flux cannot.

We further compare the propagation of rupture fronts and shear stress time history under the influence of different numerical fluxes and meshes in Figure 6. The results in four cases are compared, namely: symmetric mesh & upwind flux, symmetric mesh & mixed flux, asymmetric mesh & upwind flux, and asymmetric mesh & mixed flux. The rupture fronts in Figure 6a almost overlap; a zoom-in as in Figure 6b shows the max-

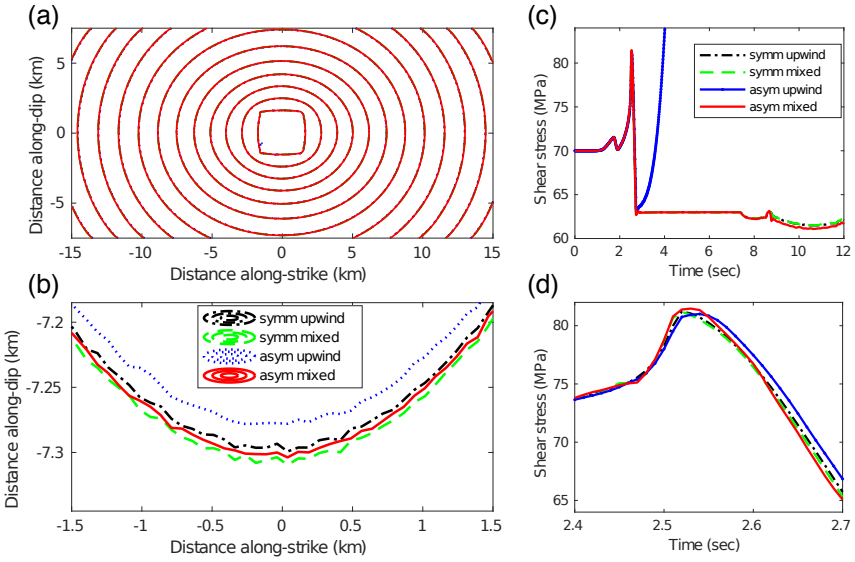

Figure 6. (a) Comparison of rupture fronts calculated by different meshes (symmetric or asymmetric) and different numerical fluxes (upwind or mixed); (b) Zoom-in plot of (a); (c) comparison of shear stress time series on the location (5.6, 2.3) km on the fault surface; (d) zoom-in plot of (c).

imum spatial offset of the rupture fronts is only about 30 m. Even for the problematic scheme of asymmetric mesh & upwind flux, its rupture front is close to those of others, because the problem of spatial spikes only occurs after the stress is reduced to the dynamic level, hence having little effect on the rupture front itself. We selected one station on the fault surface to compare the shear stress time series of the four methods. Clearly, the application of the mixed flux, even with the asymmetric mesh, successfully converges the stress time series as opposed to the upwind flux method (Figure 6c). Overall, the fault ruptures calculated by the mixed flux are slightly faster than those calculated by the upwind flux (Figure 6b, 6d). It may be related to the dissipation of the upwind flux, which numerically damps the propagation of the rupture. Nevertheless, the difference between them is insignificant (the maximum time shift in Figure 6d is about 0.02 s).

The geometry of the TPV3 model is relatively simple compared to natural faults with complex fault geometries. By adding two extruded layers, the pairs of elements adjacent to the fault surface are completely symmetric, and the use of the upwind flux is sufficient in this case to prohibit spatial oscillations. In our experience, even with slightly asymmetric meshes, maintaining $r_v < 1.5$ can generally produce satisfactory results using upwind flux. However, for more complex fault geometry it is more challenging to generate nearly symmetric mesh with $r_v < 1.5$. Therefore, the mixed flux method becomes crucial and necessary in scenarios of $r_v > 1.5$, as illustrated in the example below.

The second example is a thrust fault in half space modified from TPV3 by adding a free surface and the dipping geometry. The initial stress and frictional parameters are similar to TPV3. The fault plane is 30 km along-strike and 15 km along-dip with a dipping angle of 15°. The initial stress is 70 MPa in the down-dip direction and 0 MPa in the strike direction. The nucleation zone is located in the center of the fault plane with an area of 3 km by 3 km and initial stress of 85 MPa. The initial normal stress is 120 MPa on the entire fault. The friction parameters are $\mu_s = 0.7$, $\mu_d = 0.5$, $D_c = 0.5$ m. Because of the free surface and the low dip angle (15°), it is impossible to generate a symmetric mesh and challenging to generate a nearly symmetric mesh ($r_v < 1.5$). We gen-

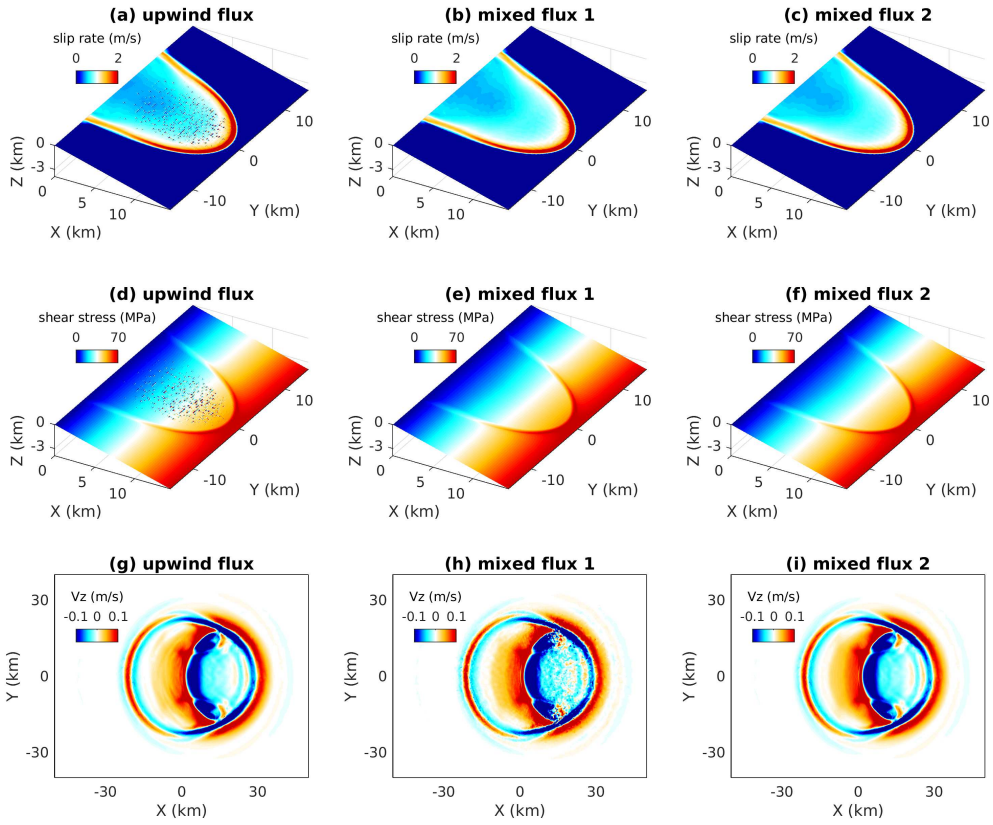

Figure 7. Comparison of TPV3 results using different types of numerical fluxes. Left column: upwind flux; middle column: mixed flux 1 (Figure 4a); right column: mixed flux 2 (Figure 4b). first row: slip rate snapshot at 5 s; second row: shear stress snapshot at 5 sec; third row: particle velocity component Vz on the ground surface at 10 sec.

erated the mesh using Gmsh (Geuzaine & Remacle, 2009). There are 18% elements with $r_v > 1.5$ adjacent to the fault surface (11,624 fault faces in total) and the maximum r_v is ∼12 due to the low dip angle (15°). The edge length of the elements near the fault is 300 m, and is coarsened to 6 km at the domain boundary. We use the spatial order of $O = 4$ for the simulations.

We first use the upwind flux to simulate the rupture process. As shown in Figure 7a and 7d the "spatial spikes" occur in both the slip rate and shear stress snapshots. With the adoption of the mixed flux, the spatial spikes are completely removed. The snapshots on the fault surface calculated by the two mixed flux approaches (as introduced in Figure 4) are almost identical, indicating that the difference between the two strategies is insignificant for the rupture process.

However, as introduced in section 3.1, the upwind flux scheme is more advantageous than the central flux scheme in suppressing the artificial high-frequency oscillations. Using the central flux for all the continuous boundaries (Figure 4a) removes the spatial spikes (compare Figure 7a and Figure 7b, or Figure 7d and Figure 7e), but the artificial high-frequency oscillations emerges in the far-field ground motion (compare Figure 7g and 7h). This is because the central flux is theoretically non-dissipative (Hesthaven & Warburton, 2008). We found that the central flux at the fault-intersecting faces only is sufficient to suppress the spatial spikes, whereas upwind flux applied at the rest of the continuous boundaries is effective at suppressing the artificial spurious high-frequency oscillations (Figure 4b). Therefore, we propose a more advantageous mixed flux approach (mixed flux 2, Figure 4b) which removes the "spatial spikes" while suppressing the spurious "high-frequency oscillations". As shown in Figure 7i, the wave field calculated by the mixed flux 2 is also free of spurious high-frequency oscillations, similar to the result of upwind flux (Figure 7g). Therefore, the scheme of mixed flux 2 should be the best choice for modeling dynamic rupture process using DG method with an asymmetric mesh.

4 Numerical Verification

Our proposed mixed flux DG method can be applied to simulate dynamic rupture processes with complex fault geometries, heterogeneous materials, off-fault plasticity, roughness, thermal pressurization, and various versions of fault friction laws. In this section, we benchmark our simulation results with solutions from the SCEC/USGS Rupture Code Verification project (Harris et al., 2009, 2018). In the following, we present the benchmark results for two selected problems, and refer the readers to the Supporting Information for additional cases (Text S5 and Figures S2-S8 in S1).

4.1 TPV24: Branching Fault

The first benchmark problem is the SCEC/USGS dynamic rupture model TPV24, which is a branching fault in half space (Harris et al., 2018). The TPV24 model has a vertical planar main fault of 40 km × 20 km and a vertical planar branching fault (12 km × 20 km) that intersects with the main fault at an angel of 30° (Figure 8). A circle nucleation patch (with a radius of 1.5 km) is located at −8 km and 10 km, respectively, in the along-strike and along-dip directions of the main fault. The material is homogeneous with $V_p = 6$ km/s, $V_s = 3.464$ km/s, and $\rho = 2.67$ g/cm^3. The stress component of the fault surface varies with depth. The static friction coefficient is 0.18, the dynamic friction coefficient is 0.12, and the characteristic slip distance is 0.3 m. The grid size near the fault is 300 m ($O = 4$), which gradually increases to 5 km at the boundary of the model domain (Figure 8a).

Figure 8b shows that rupture nucleates on the main fault and propagation continues on both the main and branch faults. The rupture propagates faster on the branch fault than on the main fault, because the traction forces projected onto the branch fault

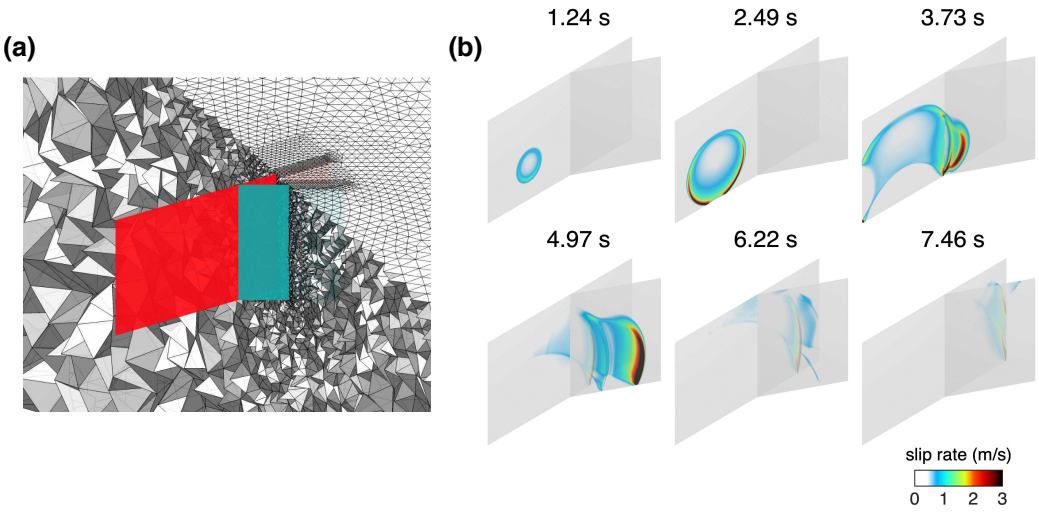

Figure 8. (a) Close-up and cutaway views of the unstructured tetrahedral mesh of the branch fault model (TPV24). The red plane is the (vertical) main fault, 28 km along strike and 15 km along dip; the cyan plane is the (vertical) branch fault, with a length of about 12 km and a depth of about 15 km; the angle between the two fault planes is 30°. The element on the fault plane have a side length of 300 m, and away from the fault, the element side length is coarsened to 5 km at the domain boundary. The mesh contains a total of 845,369 tetrahedron. (b) Snapshots of simulated slip rates.

are larger given the fault geometry and background stress orientations. Supershear rupture front is clearly shown along the branch fault at $t = 4$ s in Figure 8b and Figure 9b.

We benchmark our numerical results with those using the modal DG method (ADER-DG) (Pelties et al., 2012), by comparing rupture front contours and synthetic seismograms on the fault, shown in Figure 9a-b and Figure 9c, respectively. Our results are clearly in good agreement with those calculated by the ADER-DG, and the differences between the two methods are within acceptable tolerances of numerical errors (within 1% of relative error of rupture time). This comparison demonstrates that our method can properly simulate dynamic rupture along branching faults.

4.2 Rate-State Friction Law with Thermal Pressurization

Our second benchmark example is the SCEC/USGS TPV105-3D, which assumes fault friction follows the strong velocity-weakening rate-state friction law and includes thermal pressurization (TP) as an additional weakening mechanism (Harris et al., 2018). We adopt the "pseudo-spectral" method introduced by Noda and Lapusta (2010) to implement the governing equations of temperature and pore pressure changes. The same method is implemented in SeisSol.

The TPV105-3D model consists of a vertical strike-slip fault of a size of 44 km by 22 km embedded in a homogeneous half space (Figure 10a). The fault is governed by the rate and state friction law with flash heating (Di Toro et al., 2004) and is further weakened by the reduction of effective normal stress due to the pore pressure increase from shear heating (Andrews, 2002; Noda & Lapusta, 2010). The velocity weakening/strengthening region is set by the spatial heterogeneous friction parameters. The rupture is initiated by a circular region with a radius of 1.5 km where the shear stress exceeds the shear strength.

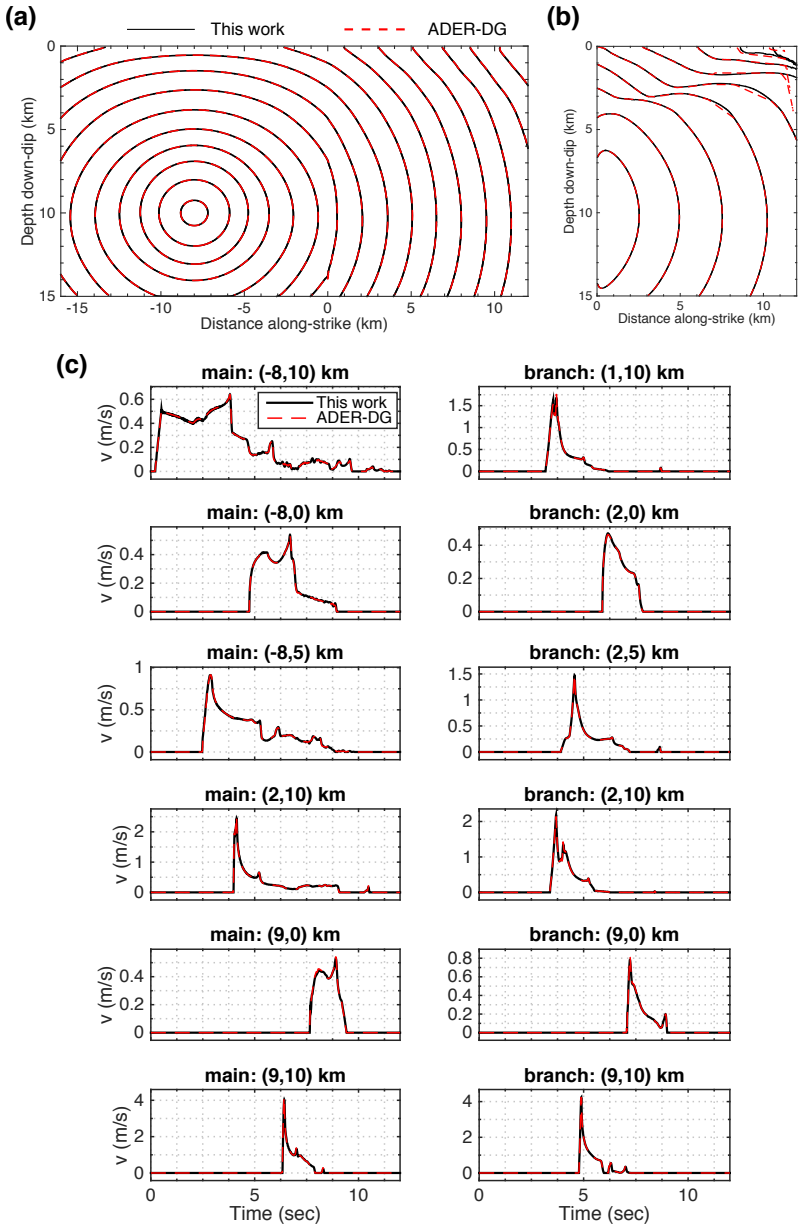

Figure 9. (a) Comparison of rupture fronts (every 0.5 s) for the main fault and (b) the branch fault calculated by our method (solid black line) and the ADER-DG method (Pelties et al., 2012) (dashed red line). (c) Comparison of the slip rate time series at different locations of the main fault plane (left column) and the branch fault plane (right column) for the branch fault model (TPV24).

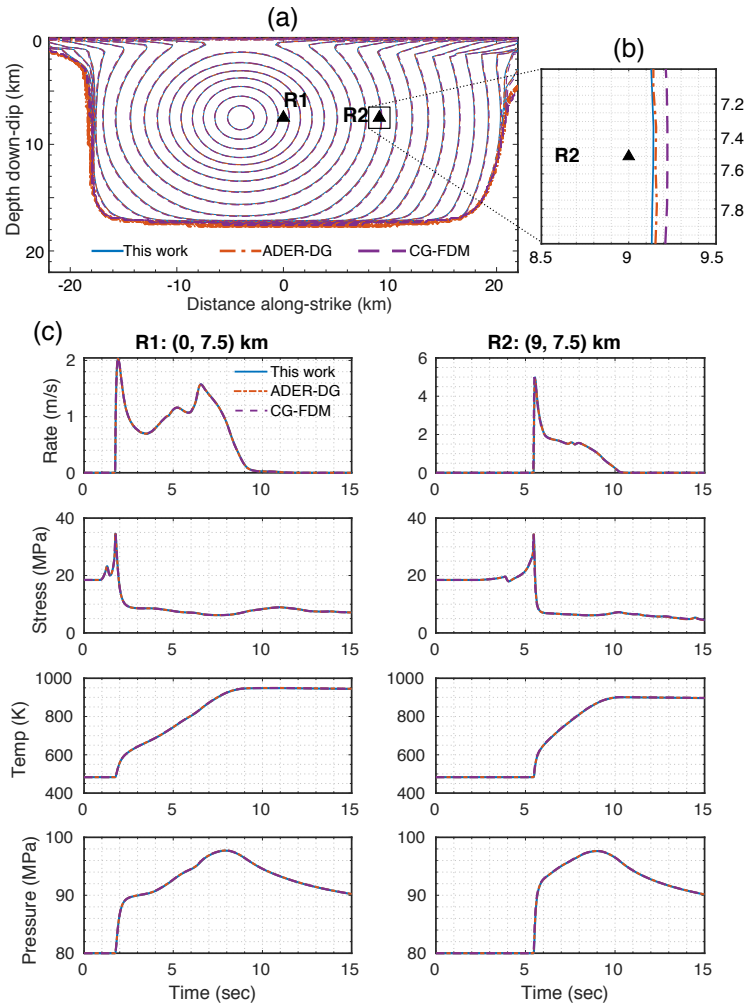

Figure 10. (a) Comparison of rupture fronts (every 0.5 s) for the TPV105-3D model calculated by our method, ADER-DG (Pelties et al., 2012) and the GPU-based CG-FDM (W. Zhang et al., 2020) (dashed red line); (b) zoomed rupture front contours in (a) near the station R2; (c) Comparison of the time series of the slip rate, shear stress, temperature and pore pressure of the two stations (R1,R2) on the fault surface.

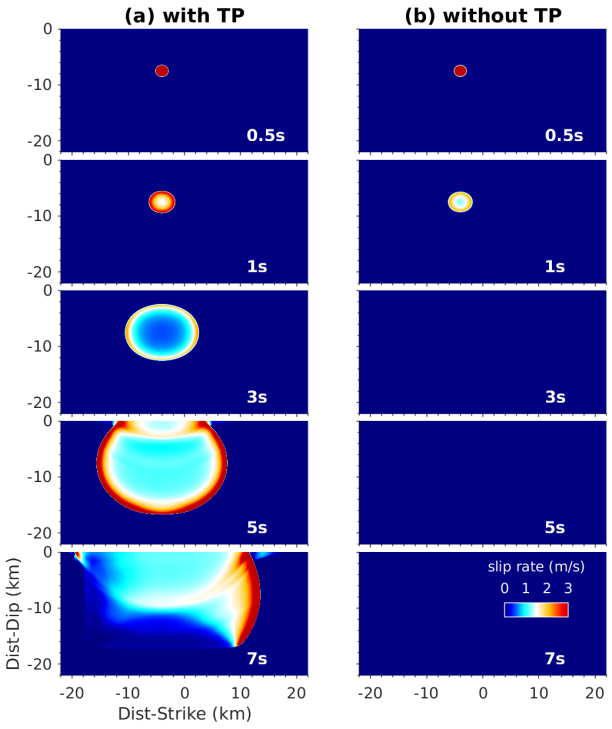

Figure 11. Comparison of snapshots of slip rates for the TPV105-3D model at different times with (a) and without (b) thermal pressurization (TP).

The full description of TPV105-3D can be found in the SCEC/USGS dynamic rupture benchmark verification website (Harris et al., 2009, 2018). We use a large computational domain with a size of 200 km by 200 km by 100 km to avoid artificial reflections from domain boundaries. The typical grid size is 200 m near the fault surface, and is gradually increased to 20 km at the domain boundary. We perform the numerical simulation using a spatial scheme of fourth-order-accuracy ($O = 4$).

We compare the rupture front contours and synthetic seismograms on the fault with those from the modal ADER-DG method (Pelties et al., 2012) and a finite difference method CG-FDM (W. Zhang et al., 2020); both solutions are available from the SCEC benchmark project website (`https://strike.scec.org/cvws/`, last accessed 2022.10.02). The typical grid size of the fault in ADER-DG is 250 m and the $O = 5$ is used. The grid size of fault in CG-FDM is 50 m and the spatial order is 4 in the bulk domain and reduced to 2 on the fault. Figure 10 shows that the rupture fronts calculated by the three methods nearly coincide, and the synthetic seismograms are also in good agreement.

To illustrate the effect of thermal pressurization, we also simulate a case identical to TPV105-3D, but without thermal pressurization. As shown in Figure 11, the introduction of thermal pressurization as an additional weakening mechanism can promote a self-arresting rupture (Figure 11a) into a runaway rupture with free-surface induced supershear rupture (Figure 11b). This suggests that thermal pressurization is an important factor for ground shaking and seismic hazard assessment.

5 2008 Wenchuan Earthquake Rupture Simulation

In this section, we demonstrate that the mixed-flux DG method can be applied to model earthquake ruptures on natural faults of complex geometry using the 2008 Mw

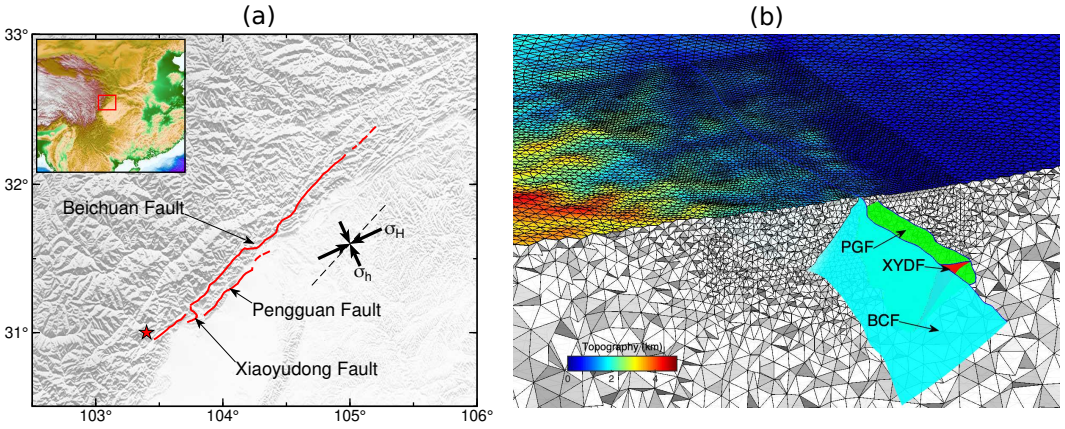

Figure 12. (a) The surface trace of the Wenchuan earthquake fault rupture. The ruptured faults include the Beichuan fault (BCF), the Pengguan fault (PGF) and the Xiaoyudong fault (XYDF). The y-axis (dashed black line) of the computational coordinate system is approximately NE 45°. The triaxial stress is assumed to be uniform in the horizontal direction. The black thick arrows indicate the direction and relative magnitude of the maximum/minimum horizontal principal stress (σ_H and σ_h). (b) Close-up and cross-sectional views of the unstructured tetrahedral mesh of the Wenchuan earthquake model. The colorbar indicates surface topography. The edge length of the elements near the fault is 2 km. Away from the fault, the cell edge lengths are coarsened to about 10 km at the domain boundary. The mesh contains a total of 1,079,239 tetrahedrons.

7.9 Wenchuan earthquake as an example. Our purpose here is to illustrate our newly developed method can properly simulate the dynamic rupture process given the fault geometry and material properties constrained by previous studies; we do not intend in this work to use the simulate results to interpret specific Wenchuan earthquake rupture mechanisms. Therefore here we do not make quantitative comparisons between our simulation results and observations. Rather, we will focus on the qualitative comparison and highlight the first-order importance of fault geometry.

The Wenchuan earthquake occurred in the Longmenshan thrust belt on the eastern margin of the Tibetan Plateau. Field surveys, GPS and InSAR measurements, and kinematic inversions of the rupture process show that the slip distribution of the Wenchuan earthquake is highly heterogeneous (Xu et al., 2009; Shen et al., 2009; Wan et al., 2016). For example, the southwestern part of the Beichuan fault presents thrust and right-lateral strike-slip, while its northeastern part is dominated by strike-slip. Numerical simulations have been conducted (Duan, 2010; Z. Zhang et al., 2019) to explain the observations and understand the underlying physics of the rupture process. However, the fault geometry is usually simplified due to the numerical difficulty of incorporating multiple fault segments. For example, the multi-fault system has been to the first order approximated as a planar dipping fault, and the non-uniform slip distribution explained by varying the background stress tensor along the fault strike (Duan, 2010). Alternatively, Z. Zhang et al. (2019) showed that the non-uniform slip distribution can also be reproduced with non-planar fault geometry under uniform background stress. A recent study by Tang et al. (2021) incorporated multi-fault segments and can produce simulation results (e.g., final coseismic slip distribution, surface displacement) in good agreement with GPS and InSAR measurements. However, due to the limited meshing and modeling flexibility of their numerical method (redevelopment based on the commercial software ABAQUS/Explicit), Tang et al. (2021) excluded the Xiaoyudong fault segment, which is estimated to have

experienced up to about 3 m of coseismic slip (Tan et al., 2012). Chen et al. (2013) suggests that the Xiaoyudong rupture is not a passive tear fault but an active participator of slip partitioning on multiple faults within the Longmenshan thrust system. Therefore, we include the Xiaoyudong fault in the model (Figure 12a).

The 3D fault geometry is constructed based on observations from previous studies (Shen et al., 2009; Wan et al., 2016; Hubbard et al., 2010), including the Beichuan fault, the Pengguan fault, and the Xiaoyudong fault segments. We also include the surface topography effect during the simulation to account for the large differences in terrain heights (∼4 km) in this region (Figure 12). As shown in Figure 12b, we utilize an external mesh generation software CUBIT (`http://cubit.sandia.gov/`) to automatically generate tetrahedral meshes that include both topography and multi-fault geometry, and label the free surfaces and fault surfaces as boundary conditions. The rest of the boundaries are treated as interior or absorbing boundaries and are handled automatically by our program (Section 2.2). To focus on the fault geometry effect, we set a homogeneous medium (Table S1 in the Supporting Information). A linear slip-weakening friction law is adopted in the dynamic rupture simulation. The background stress field is horizontally uniform and varies only with depth. The friction and stress parameters are basically adopted from previous modeling works (Z. Zhang et al., 2019; Tang et al., 2021). We set the initial stress to be 5% above the peak stress at a circular patch of radius 8 km at depth 19 km to nucleate the rupture from the southwest end of the Beichuan fault. Detailed model parameters are listed in Table S1 in the Supporting Information. We used 256 CPU processors in Compute Canada (Beluga) for parallel computing and the total computing time is about 90 minutes.

Figure 13 shows the snapshots of simulated fault slip rate (left) and cumulative slip (right). Between 0 and 10 s, the rupture nucleated at the southwest end of the Beichuan fault and propagated toward the northeast. By the time of about 20 s, the southwest segment of the Beichuan fault accumulated up to 8 m of slip and remained the segment of the highest coseismic slip. At same time, rupture jumped across to the Xiaoyudong fault and the Pengguan fault resulting in ∼3 m of coseismic slip, while continuing to propagate along the deep part of Beichuan fault with slightly less amount of coseismic slip (Figure 13a, 20-30 s). At about 40 s, the rupture ran to the northeast end of the Pengguan fault, where it re-converged with the rupture on the Beichuan fault and continued to rupture further to the northeast. The final coseismic slip is highly heterogeneous, with the maximum slip accumulated near the nucleation section at the southwest segment of the Beichuan fault, which is consistent with the results of kinematic inversion (Shen et al., 2009; Wan et al., 2016). Because we did not rotate the direction of the principal stress field along strike (as was done in Duan (2010)) and assumed a homogeneous medium in our simulation, the non-uniform coseismic slip distribution is attributed to the complex fault geometry, highlighting its first order importance.

6 Discussions

To deal with the complex fault geometry of many natural earthquakes (e.g., the 2008 Mw 7.9 Wenchuan earthquake), we developed a nodal discontinuous Galerkin method for 3D dynamic rupture modeling. Much effort has been made in this work to make the method reliable and efficient: the modification of the upwind flux scheme (mixed flux) for reliability, parallel computing and mesh coarsening technique for computational efficiency. The mixed flux scheme is important to achieve a stable simulation when asymmetric mesh near the fault is generated. We start to discuss the underlying reasons why mixed flux is suitable to dynamic rupture problems and their possible implications.

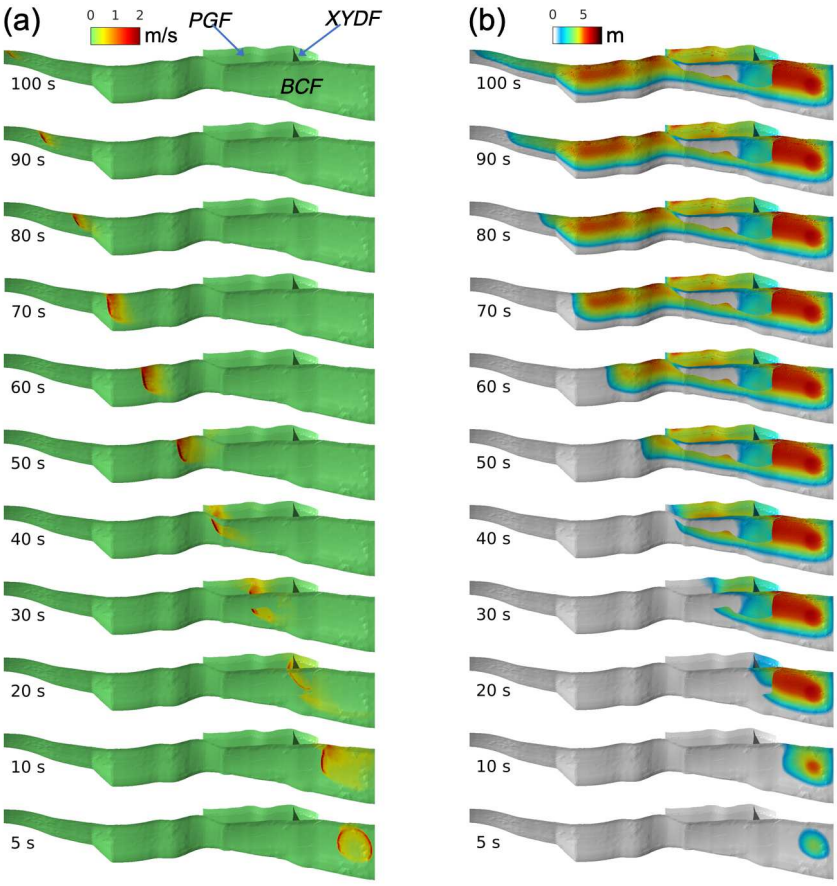

Figure 13. Snapshots of (a) slip rates and (b) cumulative slip for the dynamic rupture process of the 2018 Mw 7.9 Wenchuan earthquake.

6.1 Implications of the Mixed Flux Scheme

The choice of the numerical flux is essential to the numerical algorithms implemented with the discontinuous Galerkin method. For example, the upwind flux is universally used to deal with all boundary conditions for the wave propagation in isotropic, anisotropic, poroelastic and acoustic-elastic media (Wilcox et al., 2010; Zhan et al., 2020). While a universal adoption of a single kind of numerical flux is typically sufficient for most DG-based models with multiple types of boundary conditions, there do exist some, albeit few, studies using more than one type of numerical flux for various purposes. For example, He, Yang, Ma, and Qiu (2020) use the linear combination of Godunov flux and central flux (called "modified flux") to improve the performance of elastic wave modeling in isotropic and anisotropic media. The numerical dispersion errors are reduced thereby increasing accuracy after using the modified flux. In our work for the dynamic rupture model, the use of mixed flux is crucial as the instability problem (spatial spikes) occurs with asymmetric mesh when only the upwind flux is applied. The choice of a numerical flux suitable for specific model problems and meshes is paramount to the numerical stability of the simulation.

As discussed in Section 3, the instability of upwind flux with asymmetric mesh in the dynamic rupture model is due to the inherent numerical dissipation. Previous studies (He et al., 2019; He, Yang, & Qiu, 2020) have shown that both the mesh size and mesh shape affect the numerical dispersion and dissipation of the upwind flux. Therefore, if the mesh near the fault is highly asymmetric (e.g., $r_v > 3$), the numerical dissipation of the upwind flux will be very different on the two sides of the fault. The unbalanced dissipation error on the continuous-discontinuous fault boundaries is likely the culprit of the spatial spikes. The mixed flux scheme is numerically shown to have balanced the dissipation errors on both sides of the fault and remove the instability of spatial spikes. Our proposed mixed flux scheme may also be useful for other types of physical problems with similar mixed continuous-discontinuous boundaries, which deserve further investigation.

6.2 Parallelization and Scalability

The discontinuous Galerkin method has clearly more degrees of freedom than the traditional finite element method for the same mesh (see Figure 1b and Figure 1c). Therefore on a single process the DG method is less computational efficient than the traditional FEM. However, the DG method is much more adaptive to parallel multi-thread computation than the traditional FEMs, because the linear system of equations are solved locally (element by element) instead of globally for the traditional FEM. The solution vectors $\boldsymbol{q}$ (Equation 1) and wave impedance (Z_p and Z_s) of neighboring elements are only needed when solving for the numerical flux. Moreover, the nodal DG method only requires the solution on the element interface (rather than the whole element) to be communicated between different computing processors, therefore significantly reducing the message passing time. Our program is parallelized with Message Passing Interface (MPI) and use the METIS software (Karypis & Kumar, 1998) for the mesh partition. We test our program in the high-performance computing cluster "Narval" of Compute Canada, which consists of AMD EPYC processors (e.g., AMD Rome 7532, 7502) and high-performance interconnect of InfiniBand Mellanox HDR network (`https://docs.alliancecan.ca/wiki/Narval/en`).

We use the SCEC/USGS dynamic rupture benchmark problem TPV5 (Harris et al., 2009) as an example for the scaling test. A total of 3,093,014 tetrahedral elements are generated for the parallelization test. We evaluated the per-step running time (wall-clock time) of the program (averaged over 1000 steps) as a function of the number of processors used for the cases of spatial order of accuracy $O = 2$, 4, and 6, respectively. As shown in Figure 14b, the measured (as opposed to idealized) per-step run-time scales with

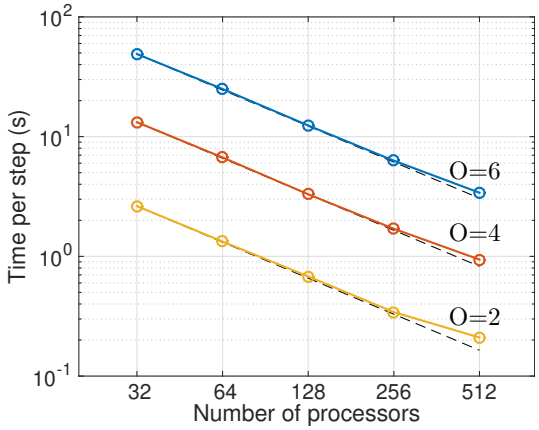

Figure 14. Parallel computation scaling test with MPI, using the TPV5 benchmark problem (Harris et al., 2009). The black dotted line is the ideal scaling, the blue, orange, and yellow curves represent the measured parallel scaling at the spatial order of accuracy $O = 2$, 4, 6, respectively.

the number of processors at nearly the ideal scaling from 32 to 256 processors. The scaling slightly deviates from the ideal scaling at 512 processors, mostly due to the increase in message passing time for the large number of processors. At 512 processors, the highest order ($O = 6$) simulation performs the best in scalability, because the matrix multiplication in Equation S19 (Text S2 in Supporting Information S1) is more time-consuming than the calculation of the numerical flux, resulting in a smaller percentage of time for message passing. We expect the good parallel scaling to extend to even larger number of processors at relatively high order of simulations.

6.3 Effects of Mesh Coarsening

One of the most important advantages of tetrahedral mesh is its flexibility to allow a great degree of mesh coarsening, which significantly reduces the number of mesh elements thereby the computation time. Here we provide a quantitative discussion of the effects of mesh coarsening for the information of future users of our method. We use the SCEC/USGS dynamic rupture benchmark problem TPV5 (Harris et al., 2009) as an example for testing the effects of mesh coarsening. The mesh size on the fault surface is fixed as $l_f = 200$ m to well resolve the rupture process. The whole computational domain is sufficiently large (100 km by 100 km by 50 km) to avoid spurious reflected waves. The maximum mesh size l_M is on the domain boundary. When the domain size is fixed, the mesh will be gradually coarsened (e.g., in linear or quadratic increment) from l_f on the fault to l_M on the domain boundary. As shown in Figure 15a, we define another parameter l (e.g., $l = 5l_f$) to keep the uniform element size of l_f near the fault surface within a finite thickness zone of $2l$. l is a useful parameter to control the mesh coarsening, especially when a very large computational domain is required. As discussed in Barall (2009), in which a hexahedral mesh is adopted, at least a four times of cell size distance (i.e., $l = 4l_f$) is required to ensure accuracy. In general, l_M and l control the gradient of mesh coarsening. We use $O = 3$ to perform the modeling.

We use the combinations of the parameters $l = l_f$, $5l_f$ and $l_M = 2$ km, 10 km, yielding four cases: C1-C4, as shown in Figure 15. C1 has the strongest coarsening while C4 has the weakest coarsening. We first compare the slip rate time histories on the fault at a station 7.5 km away from the nucleation patch. As shown in Figure 15b, C2-C4 coincide with each other, even on the sub-second time scale. While C1 is slightly faster (∼0.05

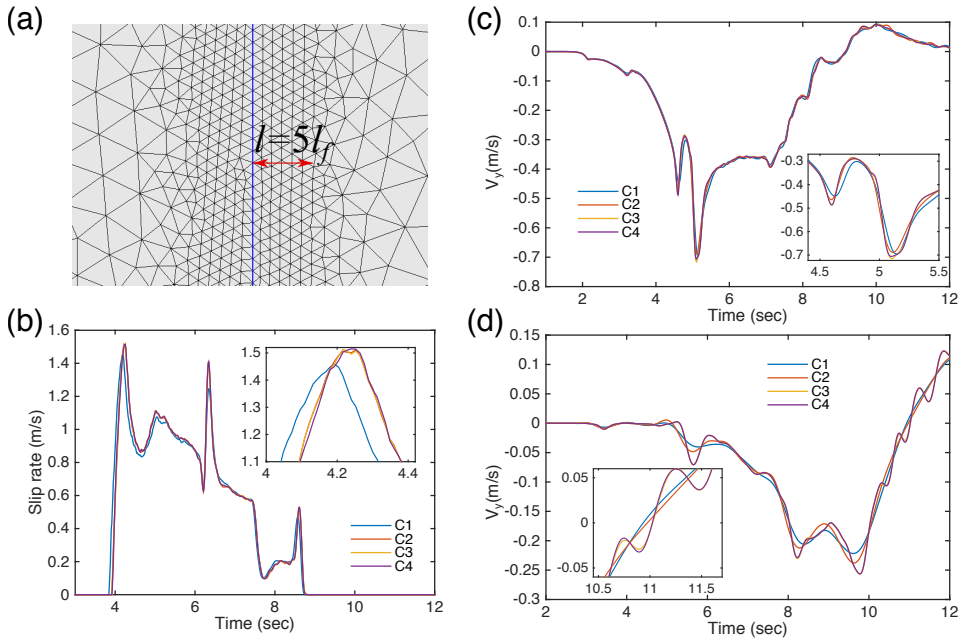

Figure 15. (a) Mesh coarsening near the fault. Mesh size is equivalent to l_f within the distance $l = 5l_f$ on each side of the fault, and increases with distance from the fault toward the domain boundary with the maximum size l_M. (b) Comparison of fault slip rate time history on the fault at (strike, dip) = (7.5, 7.5) km. C1-C4 indicates four cases: C1) $l = l_f$, l_M = 10 km, with 264,698 tetrahedrons; C2) $l = 5l_f$, l_M = 10 km, with 712,463 tetrahedrons; C3) $l = l_f$, l_M = 2 km, with 1,536,655 tetrahedrons; C4) $l = 5l_f$, l_M = 2 km, with 2,120,224 tetrahedrons. (c) comparison of the seismograms of the V_y component (parallel to fault strike). The station is on the free surface, the location is (3, 7.5) km on the fault normal and the strike direction. (d) same with (c) but with a different location of (15, 7.5) km.

s or 1%) than C2-C4. The peak value difference between C1 and C2-C4 is ∼0.1 m/s (7%). The comparison suggests while a direct coarsening from l_f to a very large mesh size at the domain boundary (e.g., $l_M = 50l_f$ = 10 km) is not sufficient for the high-accuracy requirement, using several elements with uniform size near the fault (e.g., $l = 5l_f$) will greatly improve the accuracy. Nevertheless, the difference between C1 and C2-C4 is still minor, indicating the mesh coarsening has little effect on modeling results here. The difference will be further reduced as the order-of-accuracy increases (e.g., $O = 4$).

Next, we compare the synthetic seismograms at surface stations near and far from the fault. For the station at 3 km fault-normal distance, the difference between the four cases is insignificant (Figure 15c). However, for the station at 15 km fault-normal distance, there are visible differences in the four cases (Figure 15d). C1 is similar to C2 and C3 almost coincides with C4. The result shows that the parameter l_M has a great effect on the far-field seismogram. A larger element has more numerical dissipation, which will have a filtering effect on the seismogram, therefore less high-frequency information of the C1 and C2 seismograms than those of C3 and C4. Despite the difference in the high-frequency information, the general shape of the seismograms of C1-C4 remains similar. Our comparison suggests that even a very strong mesh coarsening will not greatly affect the results, although we need to take a cautionary note in high-frequency waveform interpretations.

6.4 Limitations and Future Works

Absorbing boundary treatment is very important for volumetric numerical methods such as FDM, FVM and FEM. In all the benchmark problems and the Wenchuan earthquake simulation case discussed above, we adopted the first-order absorbing boundary condition based on the numerical flux (Equation 6). More advanced absorbing boundary treatment such as the perfectly matched layer (PML) (Berenger, 1994), can be implemented in the current framework. However, thanks to the strong coarsening ability of the tetrahedral mesh, the use of PML became less urgent as we can accommodate a larger computational area without significantly increasing the number of mesh elements. By comparing the results with those of other methods, it can be shown that the fault rupture process we calculated is basically not affected by the spurious reflected waves. However, for some special cases, for example, when the aspect ratio of the computational domain is very large, the near-grazing incident waves (W. Zhang & Shen, 2010) are difficult to absorb with the first-order absorbing boundary condition. In this case, it is necessary to use the PML technique to deal with spurious reflected waves.

The method is currently limited to the first-order mesh, i.e., the straight edge mesh. The curved fault surface is represented by the piecewise linear segments. Using straight-edged elements will inevitably result in a kink-like geometry of adjacent elements. This kink-like geometry creates stress concentrations that cause the stress snapshot to appear as a small amplitude spatial oscillation. Refining the grid can make this kink smaller at the expense of increased computational load. One of the natural adjustments is to use a curved mesh DG method. However, the computational and memory costs will increase due to integration on curvilinear elements in tetrahedral mesh, especially when the boundary geometry is represented by very high order polynomials in high dimensions. Future work needs to devote to the efficient implementation of the DG method based on curved meshes.

7 Conclusion

We developed a new nodal discontinuous Galerkin method to model 3D dynamic rupture problems with a fully unstructured tetrahedral mesh. A heterogeneous upwind flux scheme for the fault discontinuity boundary condition is derived based on the velocity-strain elastodynamic equation. We found that in cases of fault-bounding asymmetric mesh the universal adoption of upwind flux for all boundary conditions will lead to spatial oscillations especially in the stress components. To circumvent this problem, we proposed a new mixed flux scheme, which applies central flux only to the surfaces immediately adjacent to the fault and uses upwind flux for all other surfaces. The mixed flux scheme subtly removes the instability of spatial spikes without losing accuracy or increasing computational burden. The use of numerical fluxes in the DG scheme enables an explicit time integration scheme, making massive parallel computation easy to implement. We have successfully extended the program using MPI, and showed that the program has satisfied parallel efficiency up to $\sim$500 CPU processors. Our program still has the potential to be optimized and scaled on a larger scale on supercomputers.

We demonstrated the applicability and robustness of this new method using several SCEC/USGS dynamic rupture benchmark problems, including bimaterial faults, off-fault plasticity, thermal pressurization and complex fault geometries and various forms of friction laws. Preliminary results of the dynamic rupture process of the 2008 Wenchuan earthquake show that our method is suitable for modeling realistic earthquake ruptures considering both complex topography and multi-fault geometry. Our work provides a reliable and flexible tool to model dynamic rupture processes for complex fault geometries and heterogeneous material properties.

Acknowledgments

We thank the SCEC/USGS Spontaneous Rupture Code Verification Project (`https://strike.scec.org/cvws/`) for designing the benchmarks models and providing the dataset. Dr. Haipeng Luo and Luhong (Amy) Lu made valuable suggestions for improving the manuscript. We are very grateful to the developers of Gmsh for the meshing software. All simulations were run on supercomputers of Compute Canada (Beluga and Narval). This research was supported by the Natural Sciences and Engineering Research Council of Canada (NSERC): Strategic Grant STPGP/494141-2016, Discovery Grant RGPAS/522498-2018, Wares Science Innovation Prospectors Fund 2020 and Guangdong Provincial Key Laboratory of Geophysical High-resolution Imaging Technology (2022B1212010002).

References

Aagaard, B. T., Knepley, M. G., & Williams, C. A. (2013). A Domain Decomposition Approach to Implementing Fault Slip in Finite-Element Models of Quasi-Static and Dynamic Crustal Deformation. *Journal of Geophysical Research: Solid Earth*, *118*(6), 3059–3079. doi: 10.1002/jgrb.50217

Ando, R., & Kaneko, Y. (2018). Dynamic Rupture Simulation Reproduces Spontaneous Multifault Rupture and Arrest During the 2016 Mw 7.9 Kaikoura Earthquake. *Geophysical Research Letters*, *45*(23), 12,875-12,883. doi: 10.1029/2018GL080550

Andrews, D. J. (2002). A fault constitutive relation accounting for thermal pressurization of pore fluid. *Journal of Geophysical Research: Solid Earth*, *107*(B12), ESE 15-1-ESE 15-8. doi: 10.1029/2002JB001942

Barall, M. (2009). A grid-doubling finite-element technique for calculating dynamic three-dimensional spontaneous rupture on an earthquake fault. *Geophysical Journal International*, *178*(2), 845–859. doi: 10.1111/j.1365-246X.2009.04190.x

Benjemaa, M., Glinsky-Olivier, N., Cruz-Atienza, V. M., & Virieux, J. (2009). 3-D dynamic rupture simulations by a finite volume method. *Geophysical Journal International*, *178*(1), 541–560. doi: 10.1111/j.1365-246X.2009.04088.x

Berenger, J.-P. (1994). A perfectly matched layer for the absorption of electromagnetic waves. *Journal of Computational Physics*, *114*(2), 185-200. doi: 10.1006/jcph.1994.1159

Breuer, A., & Cui, Y. (2016). Report: 2016 SCEC project No. 16247, Increasing the Efficiency of Dynamic Rupture Simulations by Concurrently Executed Forward Runs.

Breuer, A., & Cui, Y. (2018). Report: 2018 SCEC project No. 18211, Nonlinear Earthquake Simulations Through Robust and Accurate A Posteriori Sub-Cell Limiting.

Carpenter, M. H., & Kennedy, C. A. (1994). *Fourth-order 2N-storage Runge-Kutta schemes* (Technical Memorandum (TM) No. 109112). Hampton, VA, United States: NASA Langley Research Center.

Chen, L., Ran, Y., Wang, H., Shi, X., Liu, R., & Dong, S. (2013). Paleoseismology and kinematic characteristics of the Xiaoyudong rupture, a short but significant strange segment characterized by the May 12, 2008, Mw 7.9 earthquake in Sichuan, China. *Tectonophysics*, *584*, 91-101. doi: 10.1016/j.tecto.2012.08.030

Cockburn, B., Karniadakis, G. E., & Shu, C.-W. (2012). *Discontinuous Galerkin methods: theory, computation and applications* (Vol. 11). Springer Science & Business Media.

Dalguer, L. A., & Day, S. M. (2007). Staggered-Grid Split-Node Method for Spontaneous Rupture Simulation. *Journal of Geophysical Research*, *112*(B2). doi: 10.1029/2006JB004467

Das, S. (1976). *A numerical study of rupture propagation and earthquake source mechanism* (Unpublished doctoral dissertation). Massachusetts Institute of Technology., Cambridge, MA

Das, S., & Aki, K. (1977). A numerical study of two-dimensional spontaneous rupture propagation. *Geophysical Journal International*, *50*(3), 643–668. doi: 10.1111/j.1365-246X.1977.tb01339.x

Day, S. M. (1982). Three-dimensional finite difference simulation of fault dynamics: Rectangular faults with fixed rupture velocity. *Bulletin of the Seismological Society of America*, *72*(3), 705–727. doi: 10.1785/BSSA0720030705

Day, S. M., Dalguer, L. A., Lapusta, N., & Liu, Y. (2005). Comparison of finite difference and boundary integral solutions to three-dimensional spontaneous rupture. *Journal of Geophysical Research: Solid Earth*, *110*(B12), B12307. doi: 10.1029/2005JB003813

de la Puente, J., Ampuero, J.-P., & Käser, M. (2009). Dynamic Rupture Modeling on Unstructured Meshes Using a Discontinuous Galerkin Method. *Journal of Geophysical Research*, *114*(B10), B10302. doi: 10.1029/2008JB006271

Di Toro, G., Goldsby, D. L., & Tullis, T. E. (2004). Friction falls towards zero in quartz rock as slip velocity approaches seismic rates. *Nature*, *427*(6973), 436–439.

Duan, B. (2010). Role of Initial Stress Rotations in Rupture Dynamics and Ground Motion: A Case Study with Implications for the Wenchuan Earthquake. *Journal of Geophysical Research*, *115*(B5), B05301. doi: 10.1029/2009JB006750

Dumbser, M., & Loubère, R. (2016). A simple robust and accurate a posteriori sub-cell finite volume limiter for the discontinuous Galerkin method on unstructured meshes. *Journal of Computational Physics*, *319*, 163-199. doi: 10.1016/j.jcp.2016.05.002

Duru, K., Rannabauer, L., Gabriel, A.-A., & Igel, H. (2021). A New Discontinuous Galerkin Method for Elastic Waves with Physically Motivated Numerical Fluxes. *Journal of Scientific Computing*, *88*(3), 51. doi: 10.1007/s10915-021-01565-1

Ely, G. P., Day, S. M., & Minster, J.-B. (2009). A support-operator method for 3-D rupture dynamics. *Geophysical Journal International*, *177*(3), 1140–1150. doi: 10.1111/j.1365-246X.2009.04117.x

Fu, H., He, C., Chen, B., Yin, Z., Zhang, Z., Zhang, W., ... Chen, X. (2017). 18.9-Pflops nonlinear earthquake simulation on Sunway TaihuLight: enabling depiction of 18-Hz and 8-meter scenarios. In *Proceedings of the International Conference for High Performance Computing, Networking, Storage and Analysis on - SC '17* (pp. 1–12). Denver, Colorado: ACM Press. doi: 10.1145/3126908.3126910

Galvez, P., Ampuero, J.-P., Dalguer, L. A., Somala, S. N., & Nissen-Meyer, T. (2014). Dynamic earthquake rupture modelled with an unstructured 3-D spectral element method applied to the 2011 M9 Tohoku earthquake. *Geophysical Journal International*, *198*(2), 1222–1240. doi: 10.1093/gji/ggu203

Geuzaine, C., & Remacle, J.-F. (2009). Gmsh: A 3-D finite element mesh generator with built-in pre- and post-processing facilities. *International Journal for Numerical Methods in Engineering*, *79*(11), 1309-1331. doi: 10.1002/nme.2579

Harris, R. A., Barall, M., Aagaard, B., Ma, S., Roten, D., Olsen, K., ... Dalguer, L. (2018). A Suite of Exercises for Verifying Dynamic Earthquake Rupture Codes. *Seismological Research Letters*, *89*(3), 1146–1162. doi: 10.1785/0220170222

Harris, R. A., Barall, M., Archuleta, R., Dunham, E., Aagaard, B., Ampuero, J. P., ... Templeton, E. (2009). The SCEC/USGS Dynamic Earthquake Rupture Code Verification Exercise. *Seismological Research Letters*, *80*(1), 119–126. doi: 10.1785/gssrl.80.1.119

He, X., Yang, D., Ma, X., & Lang, C. (2019). Dispersion–dissipation analysis of the triangle-based discontinuous Galerkin method for scalar wave equation. *Geo-*

physical Journal International, *218*(2), 1174-1198. doi: 10.1093/gji/ggz170

He, X., Yang, D., Ma, X., & Qiu, C. (2020). A modified numerical-flux-based discontinuous Galerkin method for 2D wave propagations in isotropic and anisotropic media. *GEOPHYSICS*, *85*(5), T257-T273. doi: 10.1190/geo2019-0485.1

He, X., Yang, D., & Qiu, C. (2020). Dispersion-dissipation analysis of triangular numerical-flux-based discontinuous galerkin method for elastic wave equations. *Journal of Computational Physics*, *418*, 109630. doi: 10.1016/j.jcp.2020.109630

Hesthaven, J. S., & Warburton, T. (2008). *Nodal Discontinuous Galerkin Methods* (Vol. 54; J. E. Marsden, L. Sirovich, & S. S. Antman, Eds.). New York, NY: Springer New York. doi: 10.1007/978-0-387-72067-8

Hubbard, J., Shaw, J. H., & Klinger, Y. (2010). Structural Setting of the 2008 Mw 7.9 Wenchuan, China, Earthquake. *Bulletin of the Seismological Society of America*, *100*(5B), 2713-2735. doi: 10.1785/0120090341

Kaneko, Y., Lapusta, N., & Ampuero, J.-P. (2008). Spectral element modeling of spontaneous earthquake rupture on rate and state faults: Effect of velocity-strengthening friction at shallow depths. *Journal of Geophysical Research: Solid Earth*, *113*(B9), B09317. doi: 10.1029/2007JB005553

Karypis, G., & Kumar, V. (1998). A fast and high quality multilevel scheme for partitioning irregular graphs. *SIAM Journal on Scientific Computing*, *20*(1), 359-392. doi: 10.1137/S1064827595287997

Kozdon, J. E., & Dunham, E. M. (2013). Rupture to the Trench: Dynamic Rupture Simulations of the 11 March 2011 Tohoku Earthquake. *Bulletin of the Seismological Society of America*, *103*(2B), 1275–1289. doi: 10.1785/0120120136

Kozdon, J. E., Dunham, E. M., & Nordström, J. (2012). Interaction of Waves with Frictional Interfaces Using Summation-by-Parts Difference Operators: Weak Enforcement of Nonlinear Boundary Conditions. *Journal of Scientific Computing*, *50*(2), 341–367. doi: 10.1007/s10915-011-9485-3

Kozdon, J. E., Dunham, E. M., & Nordström, J. (2013). Simulation of Dynamic Earthquake Ruptures in Complex Geometries Using High-Order Finite Difference Methods. *Journal of Scientific Computing*, *55*(1), 92–124. doi: 10.1007/s10915-012-9624-5

Käser, M., & Dumbser, M. (2006). An arbitrary high-order discontinuous Galerkin method for elastic waves on unstructured meshes - I. The two-dimensional isotropic case with external source terms. *Geophysical Journal International*, *166*(2), 855–877. doi: 10.1111/j.1365-246X.2006.03051.x

LeVeque, R. J. (2002). *Finite volume methods for hyperbolic problems*. Cambridge University Press. doi: 10.1017/CBO9780511791253

Ma, S., & Archuleta, R. J. (2006). Radiated seismic energy based on dynamic rupture models of faulting. *Journal of Geophysical Research: Solid Earth*, *111*(B5), B05315. doi: 10.1029/2005JB004055

Madariaga, R. (1976). Dynamics of an expanding circular fault. *Bulletin of the Seismological Society of America*, *66*(3), 639–666. doi: 10.1785/BSSA0660030639

Noda, H., & Lapusta, N. (2010). Three-dimensional earthquake sequence simulations with evolving temperature and pore pressure due to shear heating: Effect of heterogeneous hydraulic diffusivity. *Journal of Geophysical Research: Solid Earth*, *115*(B12). doi: 10.1029/2010JB007780

Oglesby, D. D., Archuleta, R. J., & Nielsen, S. B. (2000). The three-dimensional dynamics of dipping faults. *Bulletin of the Seismological Society of America*, *90*(3), 616–628. doi: 10.1785/0119990113

Pelties, C., de la Puente, J., Ampuero, J.-P., Brietzke, G. B., & Käser, M. (2012). Three-dimensional dynamic rupture simulation with a high-order discontinuous Galerkin method on unstructured tetrahedral meshes. *Journal of Geophysical Research: Solid Earth*, *117*(B2), B02309. doi: 10.1029/2011JB008857

Qian, F., Wu, B., Feng, X., & Zhang, H. (2019). 3D numerical simulation of dynamic ruptures on complex fault systems by BIEM with unstructured meshes. *Chinese Journal of Geophysics (in Chinese)*, *62*(9), 3421-3431. doi: 10.6038/cjg2019M0642

Shen, Z.-K., Sun, J., Zhang, P., Wan, Y., Wang, M., Bürgmann, R., ... Wang, Q. (2009). Slip maxima at fault junctions and rupturing of barriers during the 2008 Wenchuan earthquake. *Nature Geoscience*, *2*(10), 718–724. doi: 10.1038/ngeo636

Si, H. (2015). Tetgen, a delaunay-based quality tetrahedral mesh generator. *ACM Trans. Math. Softw.*, *41*(2). doi: 10.1145/2629697

Tago, J., Cruz-Atienza, V. M., Virieux, J., Etienne, V., & Sánchez-Sesma, F. J. (2012). A 3D hp-adaptive discontinuous Galerkin method for modeling earthquake dynamics. *Journal of Geophysical Research: Solid Earth*, *117*(B9), B09312. doi: 10.1029/2012JB009313

Tan, X., Yuan, R., Xu, X., Chen, G., Klinger, Y., Chang, C., ... Li, K. (2012). Complex surface rupturing and related formation mechanisms in the Xiaoyudong area for the 2008 Mw 7.9 Wenchuan Earthquake, China. *Journal of Asian Earth Sciences*, *58*, 132-142. doi: 10.1016/j.jseaes.2012.06.005

Tang, R., Zhu, S., & Gan, L. (2021). Dynamic Rupture Simulations of the 2008 7.9 Wenchuan Earthquake: Implication for Heterogeneous Initial Stress and Complex Multifault Geometry. *Journal of Geophysical Research: Solid Earth*, *126*, e2021JB022457. doi: 10.1029/2021JB022457

Toro, E. F. (2009). *Riemann solvers and numerical methods for fluid dynamics: a practical introduction* (3rd ed ed.). Dordrecht ; New York: Springer. (OCLC: ocn401321914)

Ulrich, T., Gabriel, A.-A., & Madden, E. H. (2022). Stress, rigidity and sediment strength control megathrust earthquake and tsunami dynamics. *Nature Geoscience*, *15*(1), 67–73. doi: 10.1038/s41561-021-00863-5

Wan, Y., Shen, Z.-K., Bürgmann, R., Sun, J., & Wang, M. (2016). Fault geometry and slip distribution of the 2008 Mw 7.9 Wenchuan, China earthquake, inferred from GPS and InSAR measurements. *Geophysical Journal International*, *208*(2), 748-766. doi: 10.1093/gji/ggw421

Wang, T., Wei, S., Shi, X., Qiu, Q., Li, L., Peng, D., ... Barbot, S. (2018). The 2016 Kaikōura earthquake: Simultaneous rupture of the subduction interface and overlying faults. *Earth and Planetary Science Letters*, *482*, 44-51. doi: 10.1016/j.epsl.2017.10.056

Wilcox, L. C., Stadler, G., Burstedde, C., & Ghattas, O. (2010). A high-order discontinuous Galerkin method for wave propagation through coupled elastic–acoustic media. *Journal of Computational Physics*, *229*(24), 9373–9396. doi: 10.1016/j.jcp.2010.09.008

Wollherr, S., Gabriel, A.-A., & Uphoff, C. (2018). Off-fault plasticity in three-dimensional dynamic rupture simulations using a modal Discontinuous Galerkin method on unstructured meshes: Implementation, verification and application. *Geophysical Journal International*, *214*(3), 1556–1584. doi: 10.1093/gji/ggy213

Xu, X., Wen, X., Yu, G., Chen, G., Klinger, Y., Hubbard, J., & Shaw, J. (2009). Coseismic reverse- and oblique-slip surface faulting generated by the 2008 Mw 7.9 Wenchuan earthquake, China. *Geology*, *37*(6), 515-518. doi: 10.1130/G25462A.1

Ye, R., de Hoop, M. V., Petrovitch, C. L., Pyrak-Nolte, L. J., & Wilcox, L. C. (2016). A discontinuous Galerkin method with a modified penalty flux for the propagation and scattering of acousto-elastic waves. *Geophysical Journal International*, *205*(2), 1267-1289. doi: 10.1093/gji/ggw070

Ye, R., Kumar, K., de Hoop, M. V., & Campillo, M. (2020). A multi-rate iterative coupling scheme for simulating dynamic ruptures and seismic waves genera-

tion in the prestressed earth. *Journal of Computational Physics*, *405*, 109098. doi: 10.1016/j.jcp.2019.109098

Zhan, Q., Zhuang, M., Mao, Y., & Liu, Q. H. (2020). Unified Riemann solution for multi-physics coupling: Anisotropic poroelastic/elastic/fluid interfaces. *Journal of Computational Physics*, *402*, 108961. doi: 10.1016/j.jcp.2019.108961

Zhang, W., & Shen, Y. (2010). Unsplit complex frequency-shifted PML implementation using auxiliary differential equations for seismic wave modeling. *Geophysics*, *75*(4), T141-T154. doi: 10.1190/1.3463431

Zhang, W., Zhang, Z., Li, M., & Chen, X. (2020). GPU implementation of curved-grid finite-difference modelling for non-planar rupture dynamics. *Geophysical Journal International*, *222*(3), 2121-2135. doi: 10.1093/gji/ggaa290

Zhang, Z., Zhang, W., & Chen, X. (2014). Three-dimensional curved grid finite-difference modelling for non-planar rupture dynamics. *Geophysical Journal International*, *199*(2), 860–879. doi: 10.1093/gji/ggu308

Zhang, Z., Zhang, W., & Chen, X. (2019). Dynamic Rupture Simulations of the 2008 Mw 7.9 Wenchuan Earthquake by the Curved Grid Finite-Difference Method. *Journal of Geophysical Research: Solid Earth*, *124*(10), 10565–10582. doi: 10.1029/2019JB018630